JGR Space Physics

RESEARCH ARTICLE
10.1029/2025JA034278

Interpreting Energy-Latitude Dispersions in Mercury's Northern Magnetospheric Cusp With MESSENGER

Ryan M. Dewey[1], **Jim M. Raines**[1], **Jamie M. Jasinski**[2], **and James A. Slavin**[1]

[1]Climate and Space Sciences and Engineering, University of Michigan, Ann Arbor, MI, USA, [2]NASA Jet Propulsion Laboratory, California Institute of Technology, Pasadena, CA, USA

Key Points:

- Energy-latitude dispersions are common to Mercury's northern cusp and are spatial structures produced from steady magnetosphere conditions
- Fitting dispersions yields the distances to the open-closed boundary and to the reconnection site, probing Mercury's solar wind coupling
- Dispersions reveal that Mercury's dayside magnetosphere structure can be decoupled from the dayside reconnection rate

Correspondence to:
R. M. Dewey,
rmdewey@umich.edu

Citation:
Dewey, R. M., Raines, J. M., Jasinski, J. M., & Slavin, J. A. (2025). Interpreting energy-latitude dispersions in Mercury's northern magnetospheric cusp with MESSENGER. *Journal of Geophysical Research: Space Physics*, *130*, e2025JA034278. https://doi.org/10.1029/2025JA034278

Received 5 JUN 2025
Accepted 3 AUG 2025

© 2025. The Author(s).
This is an open access article under the terms of the Creative Commons Attribution License, which permits use, distribution and reproduction in any medium, provided the original work is properly cited.

Abstract We examined energy-latitude dispersions in Mercury's northern magnetospheric cusp. These systematic trends in plasma energy originate from differences in particle travel time from the dayside magnetopause reconnection site to the low altitude, high latitude cusp. Compared to other planetary magnetospheres, the small size of Mercury's magnetosphere, large relative size of the cusps, and MESSENGER's orbital geometry require careful tracking of spacecraft motion with respect to the planetary field. We incorporate this relative motion into a physical model for these dispersions and apply it to a set of MESSENGER cusp crossings with coherent dispersions. Fitting these dispersions returns the distance of the open-closed field line boundary from the cusp and the length of the field line to the reconnection site. We demonstrate that these physical parameters can be used to probe both Mercury's solar wind coupling as well as the structure of the dayside magnetosphere. From the set of crossings, we find that dispersions are common to Mercury's cusp, that they indicate that the cusp is typically located poleward of the open-closed boundary by $\sim 6 \pm 3°$ invariant latitude, and that Mercury's magnetosphere often exhibits steady conditions for multiple Dungey cycle durations at a time. Individual case studies further demonstrate that the structure of Mercury's dayside magnetosphere can be decoupled from magnetopause reconnection and that MESSENGER can cross the dayside magnetopause into open northward planetary field lines. As part of this work, we advance uncertainty quantification and fitting techniques that can be applied to other features in Mercury's magnetosphere and other planetary systems.

1. Introduction

Magnetospheric cusps are regions of recently reconnected planetary magnetic field lines open to the magnetosheath, and as such, contain shocked solar wind plasma entering the magnetosphere. Cusps are common features in planetary magnetospheres; at Mercury (e.g., Raines et al., 2014, 2022; Winslow et al., 2012; Zurbuchen et al., 2011), Earth (e.g., Lavraud & Trattner, 2021; Pitout & Bogdanova, 2021), Saturn (e.g., Arridge et al., 2016; Jasinki, Arridge, et al., 2017; Jasinski et al., 2014, 2016; Lamy et al., 2018) and Neptune (e.g., Jasinski et al., 2022; Lepping et al., 1992) these regions are at high magnetic latitudes in the dayside magnetosphere, while at Mars individual crustal fields can possess miniature cusps (e.g., Brain et al., 2003; Poppe et al., 2021; Weber et al., 2020). Recent evidence suggests that even Jupiter's internally driven magnetosphere possesses cusps formed by its interaction with the solar wind (Xu et al., 2024). In addition to planets, moons can also possess cusp regions as their global (e.g., Ganymede; Collinson et al., 2018; Kivelson et al., 1997; Paty & Winglee, 2004) or crustal (e.g., the Moon; Halekas et al., 2008; Poppe et al., 2012; Wieser et al., 2010) magnetic fields interact with the solar wind and/or their host planet's magnetosphere. Magnetosphere cusps are usually identified and defined by plasma entry into the system, even if the plasma is studied indirectly (e.g., Winslow et al., 2012).

Mercury's magnetosphere hosts perhaps the largest relative cusps in the Solar System. The planet's relatively weak intrinsic magnetic field (~1% the surface strength of Earth's; e.g., Anderson et al., 2011) and close proximity to the Sun (~an order of magnitude greater solar wind ram pressure than at 1 AU) result in a small global magnetosphere with a typical subsolar magnetopause standoff distance of only ~1,100 km (0.45 R_M) altitude (e.g., Philpott et al., 2020; Winslow et al., 2013; Zhong et al., 2015). Frequent and intense magnetic reconnection at the dayside magnetopause continuously opens the planetary magnetic field (e.g., DiBraccio et al., 2013; Gershman et al., 2013; Li et al., 2024; Slavin et al., 2012; Sun, Slavin, Smith, et al., 2020), transporting field lines —often in the form of flux transfer events (e.g., Fear et al., 2019; Imber et al., 2014; Slavin, Lepping, et al., 2010; Sun, Slavin, Smith, et al., 2020)—and their plasma over the poles and into the nightside magnetotail by magnetic tension forces and magnetosheath flows. Due to the small magnetopause standoff distance and the ability of

intense dayside reconnection to erode the dayside magnetosphere, Mercury's northern magnetospheric cusp has been observed over a wide range of magnetic latitudes by the MESSENGER spacecraft. MESSENGER, which orbited Mercury from March 2011 through April 2015, observed Mercury's northern cusp at low altitudes nearly every dayside magnetosphere pass. From 2,760 cusp crossings (Raines et al., 2022), the northern cusp is typically centered at ∼68°N and spans ∼15° in latitude but can occupy latitudes below ∼35° to as high as past the spacecraft's periapsis (∼85°). In longitude, Mercury's northern cusp is most frequently observed between magnetic local times of 9–15 hr but can be seen as far as the day-night terminator. In addition to their size and permanence, Mercury's magnetospheric cusps have been studied for their plasma precipitation and related sputtering (e.g., Raines et al., 2022; Sun, Slavin, et al., 2022), formation and internal structure (e.g., Poh et al., 2016), dependence on solar wind conditions (e.g., He et al., 2017), and remote observation signatures (e.g., Mangano et al., 2015).

An in situ signature common to planetary cusps is energy dispersions: systematic changes in the observed plasma energy by location within the cusp. Cusp dispersions are particularly common to the solar wind-driven global-dipole magnetospheres of Earth (e.g., da Silva et al., 2022; Lockwood & Smith, 1989; Reiff et al., 1977) and Saturn (e.g., Jasinski et al., 2016), where they appear as changes in energy with magnetic latitude. At these systems, energy-latitude dispersions are interpreted to originate from magnetopause reconnection (e.g., Lockwood & Smith, 1992; Rosenbauer et al., 1975): reconnection simultaneously opens planetary field lines to magnetosheath plasma entry and exposes them to transportive magnetosheath flows. As magnetosheath plasma travels along the field line toward the planet, the field line convects in latitude creating a velocity filter (time-of-flight) effect: particles with higher parallel velocities reach low altitudes sooner, corresponding to smaller field line displacement. For subsolar magnetopause reconnection, cusp energy-latitude dispersions are therefore observed as decreasing energy with increasing latitude. In contrast to these “normal” or “classical” dispersions, “reverse” or “inverse” dispersions show the opposite trend (i.e., increasing energy with increasing latitude) and are associated with high-latitude lobe reconnection (e.g., Connor et al., 2015). Given the connection between dispersions and reconnection, dispersions are often used to infer properties of the magnetopause and magnetosphere driving (e.g., Fuselier et al., 2022; Jasinski et al., 2014; Lockwood, 1995; Lockwood & Smith, 1992; Lockwood et al., 1994, 1995; Trattner et al., 2012).

To identify and interpret cusp dispersions, the minimum observed plasma energy is typically analyzed (e.g., da Silva et al., 2022; Jasinski et al., 2016; Lockwood & Smith, 1992). The average or maximum energies may also exhibit energy-latitude trends, but these trends are less well prescribed than those in the minimum energy. First, particles with non-zero pitch angle can reach low altitudes in the same travel time as field-aligned plasma but will do so with greater total energy (e.g., Burch et al., 1982). Second, while magnetosheath plasma closest to the reconnection site has the shortest distance to travel to a low-altitude spacecraft, plasma from deeper in the magnetosheath will also be streaming toward the planet; faster field-aligned plasma streaming from deeper in the magnetosheath can arrive at the same time as slower plasma starting from closer to the magnetopause. Due to these pitch angle and streaming distance effects, the spacecraft can observe plasma at higher energies well into or even throughout the cusp. In contrast, the minimum observed energy represents the longest travel time over the shortest streaming distance. Its trend in latitude provides the most restrictive bound on, and the most reliable measure of, the dispersion signature.

Although cusp dispersions have been extensively identified and studied at Earth and Saturn, they have not been widely discussed at Mercury to date. Previous studies of Mercury's northern cusp have noted apparent energy-latitude dispersions (e.g., Raines et al., 2014, 2022), but these signatures have not been rigorously identified nor analyzed. In this study, we present proton energy dispersions within a set of MESSENGER's northern cusp crossings and analyze them for information on the driving and state of the magnetosphere. We establish a framework for interpreting dispersion signatures in the Solar System's largest relative planetary cusps where spacecraft motion plays a more critical role than in the physically larger Earth and Saturn systems. Since this is the first analysis of cusp dispersions at Mercury, we focus on “classical” (decreasing minimum energy with latitude) and large-scale (involving most or all of the cusp) dispersions to build confidence in interpreting these signatures. We find that dispersions are common to Mercury's northern cusp and demonstrate this with Figure 1, which shows eight dayside magnetosphere crossings each with a coherent, large-scale “classical” dispersion in the cusp. We use “coherent” and “large-scale” to refer to the consistent slope in the minimum energy that persists through the majority (or entirety) of the cusp crossing. These examples span the orbital mission, cover different trajectories through the cusp in both latitude and local time, and highlight different magnetosheath conditions, cusp durations,

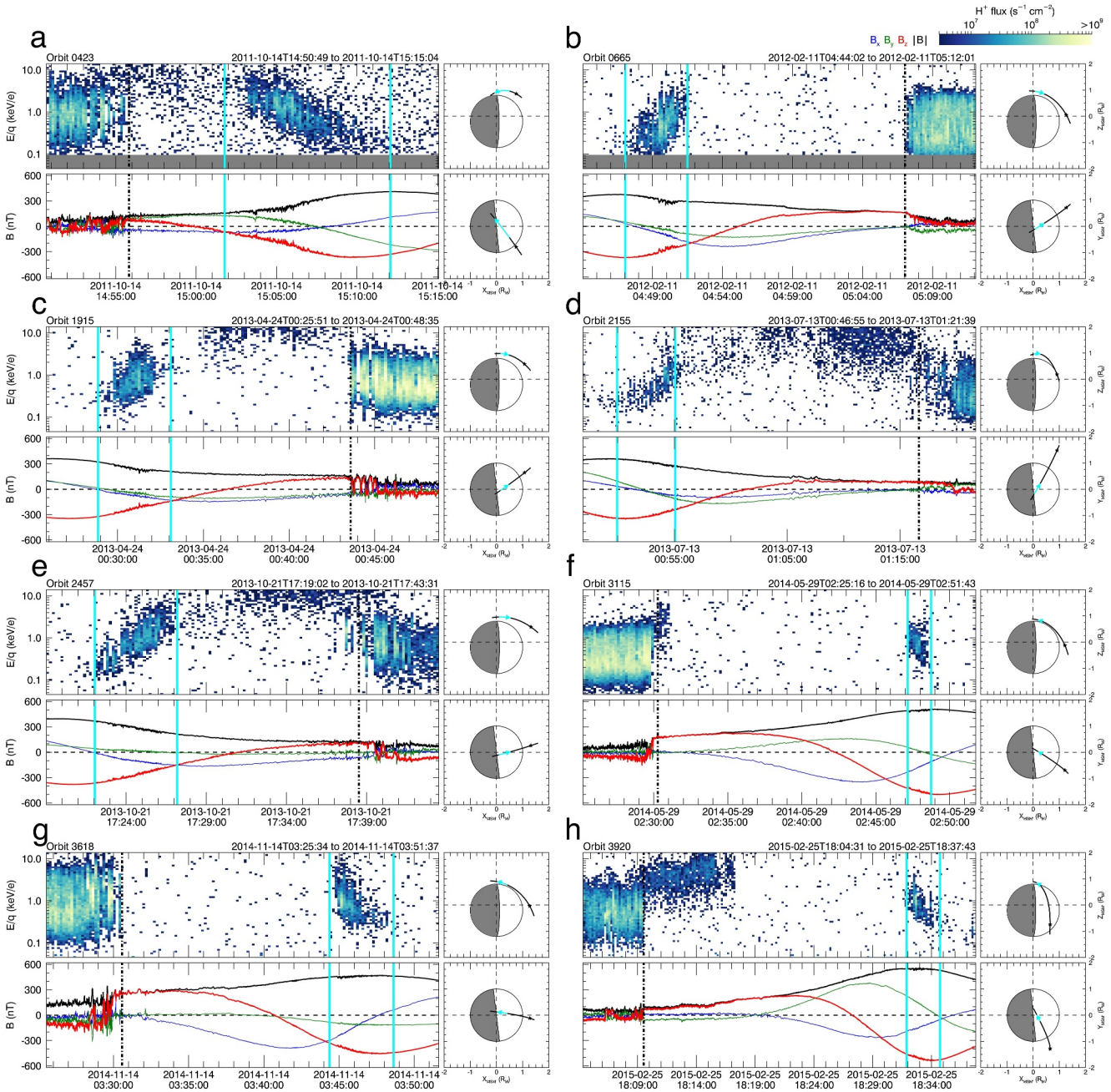


Figure 1. Examples of coherent, large-scale "classical" energy-latitude dispersions in Mercury's northern magnetospheric cusp (cyan). For each dayside magnetosphere crossing: (top left) FIPS proton differential energy flux where white indicates no counts and dark gray are energies outside the instrument's *E/q* range; (bottom left) magnetic field; and trajectory projected onto the (top right) X-$Z_{\mathrm{MSM'}}$ and (bottom right) X-$Y_{\mathrm{MSM'}}$ planes. The planetward edge of the magnetopause is indicated by the dash-dotted line and black star.

and fluxes. The remainder of the paper is organized as follows: In Section 2, we describe the data used in this study and summarize the dispersion fitting procedure (Appendix A contains the full details of the fitting methods). In Section 3, we present and discuss case study dispersion examples. In Section 4, we conclude with an eye toward future studies and BepiColombo observations.

2. Data and Methodology

2.1. Data Sources and Coordinate Frames

For this investigation, we used magnetic field and ion observations from NASA's MESSENGER spacecraft. MESSENGER orbited Mercury from March 2011 to April 2015 in an eccentric, highly inclined orbit. This orbit allowed the spacecraft to measure the northern cusp at low altitudes (<400 km) nearly every orbit; however, it never directly sampled the southern cusp. We utilize measurements from the MAG instrument (Anderson et al., 2007), a fluxgate magnetometer that measured the local vector magnetic field at 0.05 s time resolution, and the FIPS sensor (Fast Imaging Plasma Spectrometer; Andrews et al., 2007), an ion mass spectrometer. FIPS measured thermal and low-energy ions with energy-per-charge (E/q) between 0.046 and 13.6 keV/e, mass-per-charge 1–40 amu/e, and completed a sweep of its E/q steps at a nominal 10 s scan time. The sensor had a large instantaneous field of view (~1.1π sr), so although the spacecraft was three-axis stabilized, plasma flow information can still be inferred (e.g., Dewey et al., 2018, 2020). The default coordinate system we use to analyze these measurements is the aberrated Mercury solar magnetospheric (MSM') frame. This frame is centered at Mercury's dipole center with $\hat{Z}_{\mathrm{MSM'}}$ pointing northward parallel to the dipole axis. The $\hat{X}_{\mathrm{MSM'}}$ axis points anti-parallel to the incoming solar wind, which is shifted from the Sun-planet line due to Mercury's orbital motion. A solar wind speed of 400 km/s is assumed to calculate the aberration angle (typically ~6°). Finally, $\hat{Y}_{\mathrm{MSM'}}$ completes the right-handed system.

To analyze the plasma and magnetic field near the cusp with more sensitivity, we employ a local field-aligned frame of reference. This right-handed system is defined as

$$\hat{\zeta} = -\hat{b}$$

$$\hat{\chi} = \hat{Y}_{\mathrm{MSM'}} \times \hat{\zeta}$$

$$\hat{\psi} = \hat{\zeta} \times \hat{\chi}$$

The definition of $(\hat{\chi}, \hat{\psi}, \hat{\zeta})$ were chosen so that they would largely resemble $(\hat{X}, \hat{Y}, \hat{Z})_{\mathrm{MSM'}}$ in the high latitude cusp region while being aligned with the local magnetic field direction ($\hat{b}$). In these coordinates, $\hat{\zeta}$ is antiparallel to the field, $\hat{\chi}$ is perpendicular to the field and parallel to the noon-midnight direction (i.e., primary direction of convection over the pole), and $\hat{\psi}$ completes the right-handed set. Examples of this local frame are shown in Figures 2a and 2b, the dayside traversal of Figure 1c. Although the MSM' direction of $\hat{\chi}$ and $\hat{\zeta}$ change with magnetic latitude, interpretation of them is consistent in the dayside magnetosphere near local noon: $+\hat{\chi}$ represents the direction deeper into the planetary field (i.e., lower invariant latitude) and $-\hat{\zeta}$ represents the direction of plasma precipitation onto the northern planetary hemisphere. This frame is well suited to interpret convective plasma motion from the dayside to the nightside ($-\hat{\chi}$ direction) as well as plasma precipitation ($-\hat{\zeta}$) within the cusp. We transform angular FIPS observations into this local frame by averaging the magnetic field within each plasma scan to define $\hat{b}$ and its uncertainty.

In addition to organizing angular FIPS observations, we also use this frame to track MESSENGER's motion through the magnetic field. As demonstrated by the black arrows in Figure 2a the spacecraft's motion with respect to the magnetic field changes throughout its dayside magnetosphere traversal. In this example orbit, MESSENGER moves mostly perpendicular to the field along $+\hat{\chi}$ within the cusp but there is motion along the field ($\pm\hat{\zeta}$) as well. Due to the small physical scales of Mercury's magnetosphere and the potential for dayside reconnection sites to be near the cusp, the length of magnetic field lines from the spacecraft's orbit to the reconnection site may be small (<1 R_M), so spacecraft motion along the field line becomes meaningful in interpreting energy dispersions. To account for this motion, we construct the (χ, ψ, ζ) coordinate system by transforming the spacecraft's MSM' motion within each FIPS scan to a $\Delta\chi$, $\Delta\psi$, $\Delta\zeta$ based on the local $(\hat{\chi}, \hat{\psi}, \hat{\zeta})$ definition then accumulate this motion in time. For each orbit, we set the origin of this coordinate system to be the equatorward edge of the cusp crossing, as identified by Raines et al. (2022). For this example, MESSENGER's trajectory in this coordinate system is shown in Figures 2c and 2d, where within the cusp the spacecraft moves 0.29 R_M in χ, 0.18 R_M in ψ, and 0.09 R_M in ζ. Between the cusp and the magnetopause, the spacecraft moves nearly parallel to the field along ζ while its trajectory in χ reverses. During this portion of the orbit, the spacecraft moves little in ψ.

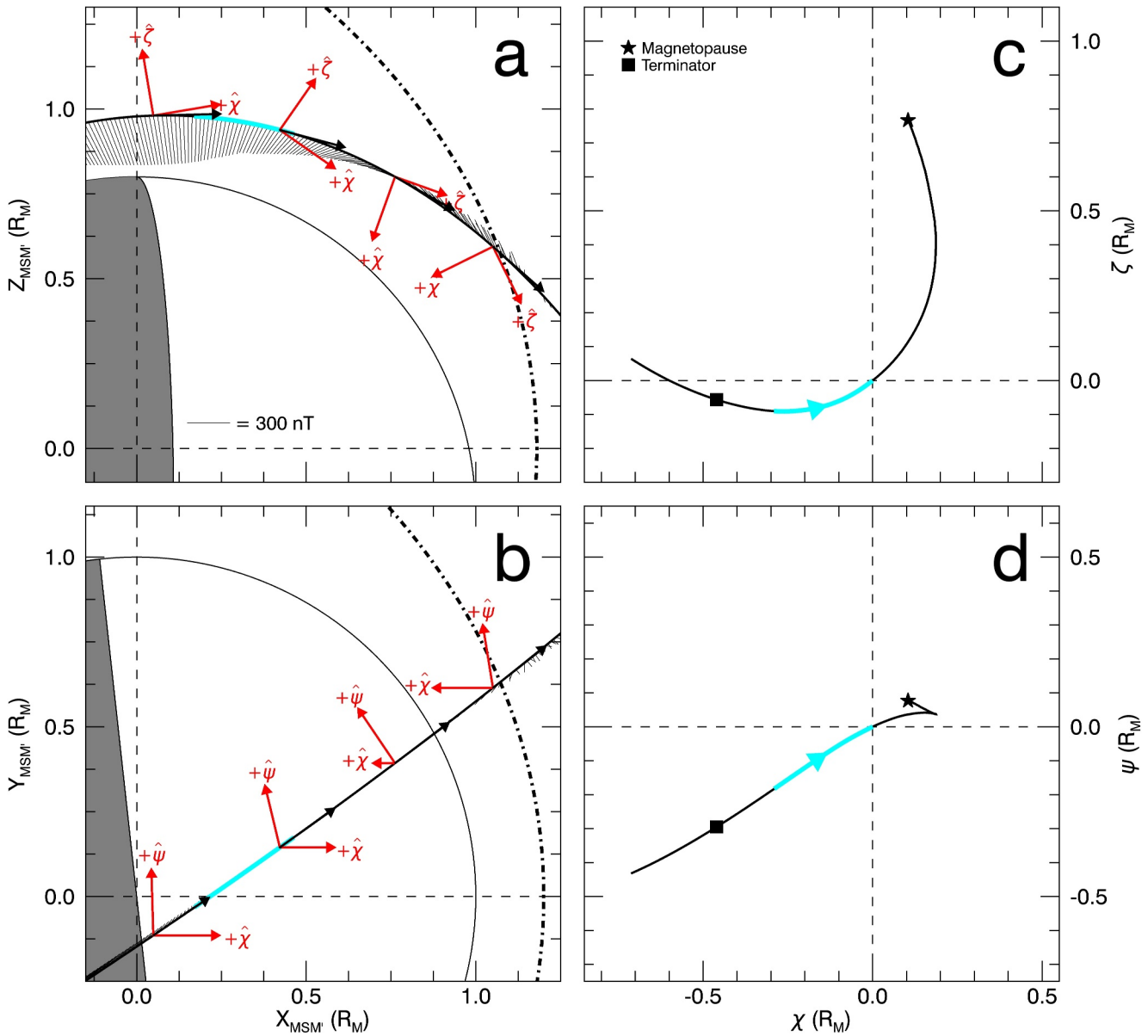


Figure 2. MESSENGER's trajectory through the dayside magnetosphere during orbit 1915 (2013-04-24T00:20 to 00:55). (a) X-$Z_{MSM'}$ projection and (b) X-$Y_{MSM'}$ projection. The cusp crossing from Raines et al. (2022) is highlighted in cyan. The thin lines indicate the direction of the average magnetic field during each FIPS scan and the dash-dotted line marks a fitted magnetopause (Winslow et al., 2013). The red arrows indicate directions of the field-aligned frame at various points in the interval, and the black arrows indicate the direction of spacecraft's motion at those points. (c) χ-ζ projection and (d) χ-ψ projection where the square marks the terminator crossing, the star the magnetopause crossing, and the arrow the spacecraft's direction of travel.

2.2. Cusp Energy Dispersion Model

To interpret cusp energy dispersions, we analyze them with the scenario described in the Introduction and depicted in Figure 3. At time $t = t_0$ magnetopause reconnection at location $(\chi, \zeta) = (\chi_0, S_0)$ opens the closed planetary field, allowing magnetosheath plasma to stream planetward while field lines convect poleward at speed u_χ. At $\zeta = 0$, the minimum observed particle speed $v_{\min}$ as a function of χ in the cusp would be:

$$\chi = \chi_0 + \frac{S_0 u_\chi}{v_{\min}} \tag{1}$$

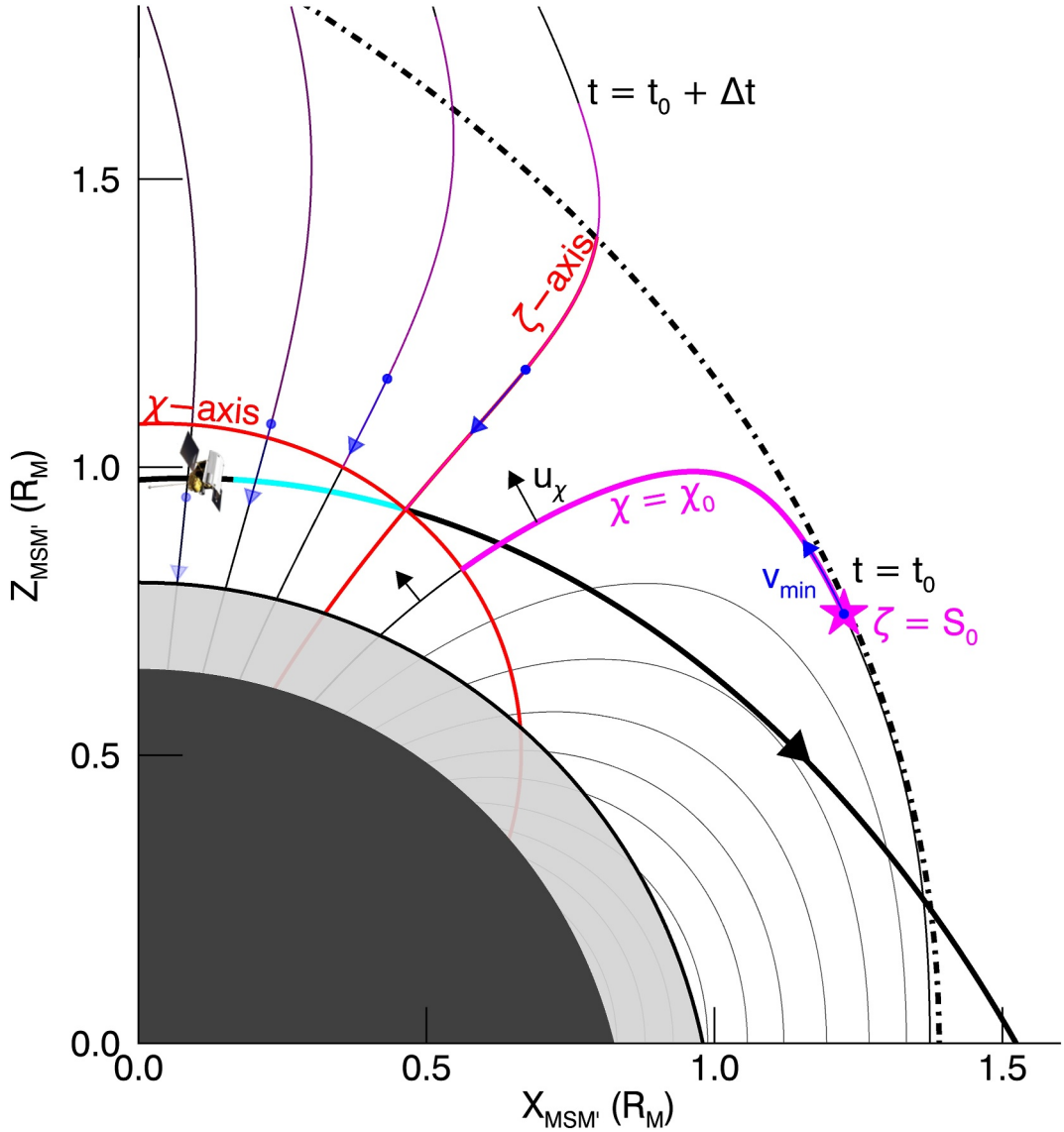


Figure 3. Schematic illustration of the cusp dispersion model. Reconnection (magenta star) occurs on the magnetopause (dash-dotted line) a distance S_0 from the χ-axis causing the field line to convect poleward at speed u_χ (thin black arrows) from its initial position χ_0. Simultaneously, magnetosheath plasma (blue) begins to stream planetward along the newly opened field line. As MESSENGER moves through the cusp (highlighted in cyan), it observes this plasma precipitation and field line convection. The equatorward edge of the cusp crossing defines the origin of the field-aligned axes (red). Mercury's core is denoted by dark gray and the mantle in semi-transparent light gray. The reconnecting field line at t_0 is located at invariant latitude Λ_0 and the equatorward edge of the cusp is at Λ_{cusp}.

This model is similar to that developed by Reiff et al. (1977). It relates the transit time of the particle along the field ($\Delta t = \Delta\zeta/v = S_0/v_{min}$) to the corresponding distance the field line has convected poleward ($\chi = \chi_0 + u_\chi \Delta t$). By definition χ_0 is the location of the open-closed boundary and S_0 is the distance along the field to the reconnection site. This model assumes no significant particle acceleration or field line stretching during the particle transit, treats magnetopause reconnection sites as wide in ψ (i.e., motion in ψ within the cusp is negligible) with convective motion dominantly along χ, and assumes an approximate steady-state or time stationary behavior of the system. We discuss stationarity in Section 3.

We adapt Equation 1 to account for the spacecraft's motion along the field within the cusp. The spacecraft motion parallel to the field effectively changes the path length particles must travel to reach the spacecraft to $\Delta\zeta = S_0 - \zeta$ (within the cusp $\zeta < 0$). Likewise, the convection speed is expected to vary along the field line.

Treating these field lines as equipotential, we expect $u_\chi \propto 1/\sqrt{B}$ from flux conservation. Both of these factors influence the dispersion signal by modifying the plasma transit time and the displacement in χ during that time, respectively. Incorporating these factors into Equation 1,

$$\chi = \chi_0 + (S_0 - \zeta)\,\frac{u_\chi}{v_{\min}}\sqrt{\frac{\tilde{B}}{B}} \tag{2}$$

where u_χ is the convection speed at reference field strength $\tilde{B}$, and B is the local strength.

The model of Equation 2 depends more explicitly on the field line convection speed u_χ. In both models, the sign of u_χ determines the type of dispersion ($u_\chi < 0$ for classic dispersions, i.e., energy decreasing with latitude) and influences the dispersion slope. Assuming frozen-in flux, u_χ can be inferred from local plasma bulk flows, however field-of-view limitations on FIPS do not always allow for this. In Equation 1, the compound parameter $S_0 u_\chi$ can be fit as a single free variable allowing χ_0 to be determined regardless of detailed knowledge of u_χ. To interpret this physically, for example, the same dispersion slope could result from either a distant reconnection site (long S_0) or rapid convection (fast u_χ). In Equation 2 the introduction of ζ complicates the functional form. To approximate the form of Equation 1, we adapt Equation 2 to

$$\chi + \zeta\,\frac{U}{v_{\min}}\sqrt{\frac{\tilde{B}}{B}} = \chi_0 + \frac{S_0 u_\chi}{v_{\min}}\sqrt{\frac{\tilde{B}}{B}} \tag{3}$$

In this expression, although ζ may not be negligible it is a first order correction to S_0 so an estimated or assumed convection speed U can be applied in place of precise convection knowledge. As described below, in the absence of a confident u_χ from FIPS we treat U as a random variable when fitting Mercury's cusp dispersions so χ_0 can still be constrained, albeit with greater uncertainty, at the expense of resolving S_0 from u_χ.

2.3. Fitting Mercury's Cusp Dispersions

We apply the dispersion model Equation 3 to MESSENGER cusp observations. We describe the steps involved in detail in Appendix A. To summarize the procedure, we first evaluate the minimum energy observed in each FIPS scan about the cusp and convert it to speed to define $v_{\min}$. Second, we constrain convective flows u_χ from FIPS angular observations if possible. If u_χ is constrained, we use $U \equiv u_\chi$ otherwise U is a random variable. We then combine these data with MAG magnetic field observations (B and $\tilde{B}$) and the field-aligned spacecraft location (χ, ζ). With these measurements we fit Equation 3 to determine χ_0 and S_0 (or $S_0 u_\chi$, depending on availability of u_χ from FIPS). At each stage of this procedure, we are careful to consider the uncertainty in the measurements as well as in the method. By employing ensemble and Monte Carlo techniques, we develop parameter distributions and produce the most robust estimates of these fit parameters by evaluating and propagating uncertainties not only related to the instrument but those related to the method itself.

We summarize these steps visually in Figure 4. Appendix A describes the components of this figure in more detail. The figure depicts FIPS observations and dispersion fitting about the cusp of orbit 1915 (i.e., the orbit in Figures 1c and 2). In panels (a)–(d), the cusp is highlighted by cyan lines with the day-night terminator to the right and the magnetic equator to the left. Time advances in this example from right to left. Figure 4a shows the FIPS proton flux as a function of field-aligned coordinate χ, and Figure 4b illustrates the ensemble approach to determining the minimum observed energy. The convective flow u_χ can be inferred during this cusp crossing, shown in Figure 4e. These measurements are used in the dispersion fitting in Figure 4c, which contains 100,000 individual fits to constrain probability distributions for χ_0 (Figure 4d) and $S_0 u_\chi$ (not shown). In Figure 4d, the red distribution uses a random U while the grey distribution uses $U \equiv u_\chi = -53 \pm 14$ km/s constrained by FIPS. The small difference between the distributions highlights how χ_0 and $S_0 u_\chi$ can still be reliably inferred from dispersions without precise knowledge of u_χ. In this example orbit, we find $\chi_0 = 0.092 \pm 0.013$ R_M and $S_0 u_\chi = -44.4 \pm 4.0$ R_M km/s.

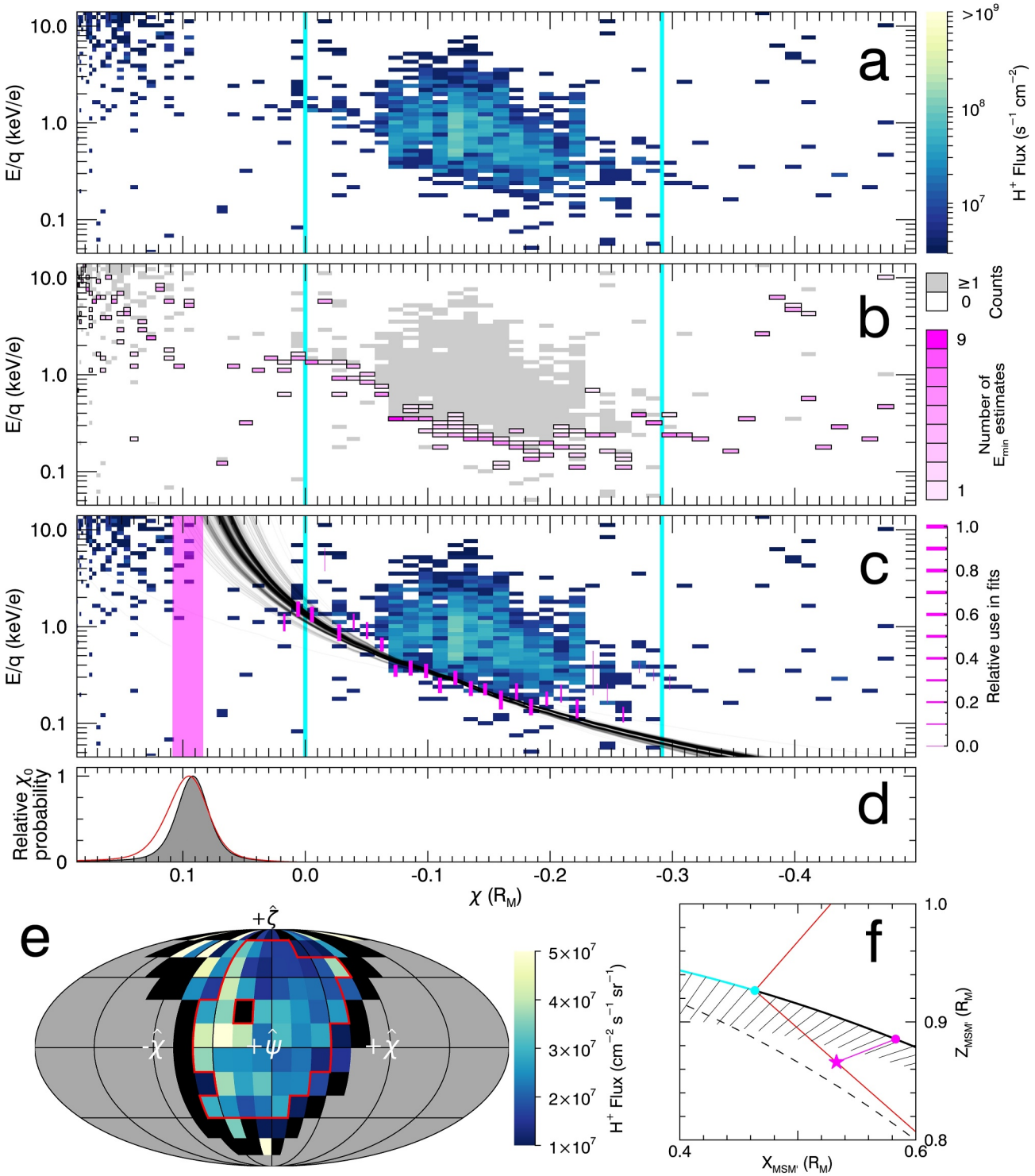


Figure 4. Illustration of determining $\overline{E}_{\min}$ and fitting the dispersion for the cusp crossing in orbit 1915. (a) Proton differential flux in the field-aligned coordinate frame. The Raines et al. (2022) cusp boundaries are marked in cyan. (b) The number of $E_{\min}$ estimates overlaid on the proton distribution where white indicates zero counts and gray indicates non-zero counts. (c) Vertical magenta bars mark $\overline{E}_{\min} \pm \delta\overline{E}_{\min}$ for scans used in dispersion fitting where the thickness indicates how frequently it was used in individual fits (transparent black traces). The shaded magenta region marks χ_0 extrapolated to MESSENGER's orbit. (d) Probability density distribution for χ_0 from the ensemble of fits. The shaded gray area is the distribution using a FIPS-constrained u_χ and the red line is from using a random U in the fitting. (e) FIPS angular flux measurements accumulated over the cusp crossing in the field-aligned frame. The region bounded in red indicates directions of high confidence. Gray indicates directions outside of the instrument's field of view during the entire cusp crossing. (f) Projection of χ_0 to MSM' space (magenta star) along the local ($+\hat{\chi}$, $+\hat{\zeta}$) directions (red) from the equatorward edge of the cusp crossing (cyan dot). The magenta line and dot project χ_0 to the spacecraft's trajectory.

2.4. Projecting χ_0 to MSM' Coordinates

One of the compelling features of the dispersion fitting in Figure 4 is that the most likely location of the open-closed field line boundary χ_0 coincides closely with the poleward edge of the high-energy dayside proton population. This population has been interpreted to be drifting ions from Mercury's magnetotail (e.g., Zhao et al., 2022), and as such, implies closed magnetic field lines. The population's edge could therefore indicate a change in magnetic field topology. However, this highlights some of the challenges in interpreting χ_0 and S_0 on a time or spatial series like this. In our dispersion model, χ_0 represents the distance from the equatorward edge of the cusp (defined to be $(\chi, \psi, \zeta) = 0$) to the open-closed field line boundary within the field-aligned coordinate system at constant field line height (i.e., along $\zeta = 0$). Since the definition of $(\hat{\chi}, \hat{\psi}, \hat{\zeta})$ changes by location, projecting a point some distance away is challenging without knowing the pointing of $(\hat{\chi}, \hat{\psi}, \hat{\zeta})$ along that path. Plotting the marginal χ_0 distribution in Figure 4d is therefore an approximation when comparing it to other features in MESSENGER's time series because the spacecraft also moves in both ψ and ζ on its way to the magnetopause as shown in Figure 2. In this orbit example, when the spacecraft is at $\chi = 0.092$ R_M, $\psi = 0.034$ R_M, and $\zeta = 0.096$ R_M so the motion in ψ is likely negligible but the motion in ζ is not. When motion in ψ is negligible (i.e., the spacecraft remains in the same convection plane) and χ_0 is small (less than the distance to the trajectory reversal in χ) we can extrapolate the dispersion fit along the spacecraft's time series and estimate when it crossed the open-closed boundary. In other words, we can find where along the spacecraft's (χ, ζ) path the dispersion fit predicts $v_{min} \rightarrow \infty$. We illustrate this as the shaded magenta region in Figure 4c. Compared to the marginal χ_0 distribution in Figure 4d this projection approach accounts for the spacecraft motion along ζ but is limited to when change in ψ in negligible. In this example, there is minimal difference between the time-projected open-closed boundary crossing in Figure 4c and the marginal χ_0 distribution in Figure 4d.

Projecting χ_0 to $\zeta = 0$ requires other approaches, one of which we demonstrate in Figure 4f. Here, we use the definition of $(\hat{\chi}, \hat{\psi}, \hat{\zeta})$ at the equatorward edge of the cusp (cyan circle) to ballistically project χ_0 into MSM' space (magenta star). Using the magnetic field observed in situ during the dayside magnetosphere transit, we then find the location in the orbit where the field pointed closest to this projected χ_0 (magenta circle). This occurred at approximately 2013-04-24T00:34:55 when MESSENGER was at $(\chi, \zeta) = (0.101, 0.108)$ R_M. This projection to $\zeta = 0$ and then back to the spacecraft orbit matches well the time-extrapolated intersection in Figure 4c.

Final support that the spacecraft crossed the open-closed boundary at $\chi \approx 0.1$ R_M comes from this orbit's particular trajectory in field-aligned coordinates. As discussed for Figure 2, MESSENGER's trajectory in χ reversed as the spacecraft traveled from the cusp to the magnetopause. In Figure 2d, the difference in ψ is small (~0.04 R_M) between the magnetopause crossing at $\chi_{MP} = 0.104 \pm 0.005$ R_M and earlier in the orbit when MESSENGER crossed the same χ. Because MESSENGER remained close to the χ-ζ convection plane we can "count" the number of field lines the spacecraft crossed as it moved deeper into the planetary field and then back out again to estimate when the spacecraft crossed the field line just interior to the magnetopause again. The local density of magnetic field lines $\propto\sqrt{B}$ from flux conservation, so by assuming a time-stationary system and integrating $\sqrt{B}\Delta\chi$ from the magnetopause to the cusp we estimate this crossing to be at 2013-04-24T00:35:02 ± 6 s when the spacecraft was located at $\chi = 0.106 \pm 0.015$ R_M. Together, these independent measures place the open-closed boundary crossing at the edge of the high-energy proton population. The fact that these multiple measures span approximately 15 min and are each in agreement is compelling evidence that the magnetosphere was in a time-stationary state.

This various mappings of χ_0 work well in this example in part because the spacecraft orbit is near the noon-midnight plane. At different magnetic local times, the spacecraft's motion in $Y_{MSM'}$ or ψ equatorward of the cusp may not be negligible. Therefore, for other orbits we use invariant latitude (Λ) mapping. At these low altitudes the field is approximately dipolar, so we use the dipole geometry of field lines to map χ_0 to the 1 R_M surface (dashed line in Figure 4f). In this example, the equatorward cusp edge is at $\Lambda_{cusp} = 62.6 \pm 0.3°$ and the open-closed boundary is at $\Lambda_0 = 57.6° \pm 0.7°$. While these projections of χ_0 are reasonable and in good agreement, projecting S_0 is more challenging given its greater distance from the spacecraft's orbit. We therefore do not project S_0 in this study. More precise mapping of both χ_0 and S_0 can be done with empirical (e.g., Korth et al., 2017; Pump et al., 2024) or physics-based (e.g., Chen et al., 2019; Exner et al., 2018; Fatemi et al., 2018; Jia et al., 2015) models of the magnetosphere.

Table 1
Cusp and Dispersion Properties From the Orbits in Figures 1 and 5–7

Orbit	χ_0 (RM)	$S_0 u_\chi$ (RM km/s)	u_χ (km/s)	S_0 (RM)	$\tilde{B}$ (nT)	E_ψ (mV/m)	Λ_0 (°)	Λ_{cusp} (°)	Δt_{cusp} (min)
423	0.206 ± 0.071	−94.4 ± 5.4	−51.1 ± 12.1	1.85 ± 0.45	245.6 ± 0.2	13 ± 3	50.0 ± 3.3	59.2 ± 0.2	10.30
665	0.039 ± 0.011	−24.7 ± 2.6	−23.8 ± 9.6	1.04 ± 0.43	302.8 ± 0.2	7 ± 3	60.0 ± 0.7	62.5 ± 0.4	4.43
868	0.057 ± 0.018	−38.6 ± 5.7	–	–	–	–	58.3 ± 1.1	62.1 ± 0.4	2.30
869	0.057 ± 0.014	−51.4 ± 5.4	–	–	–	–	58.0 ± 1.0	61.7 ± 0.4	5.15
1675	0.108 ± 0.011	−55.3 ± 3.8	−72.8 ± 17.2	0.76 ± 0.19	231.7 ± 0.2	17 ± 4	55.3 ± 0.6	61.4 ± 0.3	5.15
1676	0.212 ± 0.023	−93.0 ± 6.3	−86.1 ± 14.1	1.08 ± 0.19	253.2 ± 0.2	22 ± 4	47.4 ± 1.4	59.7 ± 0.3	5.68
1677	0.083 ± 0.024	−41.6 ± 5.6	−58.5 ± 17.6	0.71 ± 0.23	240.4 ± 0.2	14 ± 4	55.2 ± 1.4	59.9 ± 0.3	4.07
1678	0.151 ± 0.016	−62.2 ± 7.7	−50.1 ± 14.0	1.24 ± 0.38	267.3 ± 0.1	13 ± 4	53.1 ± 0.8	61.5 ± 0.3	4.43
1915	0.092 ± 0.013	−44.4 ± 4.0	−53.0 ± 14.1	0.84 ± 0.23	242.9 ± 0.2	13 ± 3	57.6 ± 0.7	62.6 ± 0.3	4.25
2155	0.127 ± 0.018	−44.6 ± 5.0	−38.5 ± 16.0	1.16 ± 0.50	300.6 ± 0.1	12 ± 5	64.5 ± 0.7	70.5 ± 0.3	5.15
2457	0.169 ± 0.029	−88.0 ± 9.1	−48.1 ± 10.2	1.83 ± 0.43	280.6 ± 0.1	13 ± 3	51.4 ± 1.7	61.0 ± 0.4	5.15
3115	0.133 ± 0.045	−66.8 ± 16.5	–	–	–	–	57.1 ± 3.0	66.8 ± 0.5	1.58
3504	0.062 ± 0.019	−27.7 ± 7.7	−43.6 ± 11.1	0.64 ± 0.26	245.7 ± 0.7	11 ± 3	55.4 ± 1.1	58.6 ± 0.3	6.57
3618	0.031 ± 0.011	−45.3 ± 5.6	–	–	–	–	58.4 ± 0.8	60.6 ± 0.5	4.25
3920	0.108 ± 0.024	−64.7 ± 9.8	–	–	–	–	56.6 ± 1.6	63.7 ± 0.6	2.83

Note. Columns from left to right: orbit number; open-closed boundary distance χ_0; compound parameter $S_0 u_\chi$; cusp convective flow u_χ determined from FIPS, if resolvable; field-line length to reconnection site S_0; reference magnetic field $\tilde{B}$; convective electric field E_ψ; projected open-closed boundary invariant latitude Λ_0; invariant latitude of the equatorward edge of the cusp Λ_{cusp}; and cusp crossing duration Δt_{cusp}.

3. Results and Discussion

We apply the cusp dispersion fitting and analysis framework above to the cusp crossings shown in Figure 1 as well as additional examples below to draw interferences about Mercury's magnetosphere. The dispersion fits from these orbits are summarized in Table 1.

3.1. Resolving Dayside Reconnection Versus Compression

The relative roles of compression and magnetic reconnection in shaping the size and structure of Mercury's dayside magnetosphere have long been discussed at Mercury (e.g., Slavin & Holzer, 1979; Slavin et al., 2014), particularly as induction effects within the planet can modify the efficacy of these processes (e.g., Glassmeier et al., 2007; Hood & Schubert, 1979; Jia et al., 2019; Suess & Goldstein, 1979). Cusp dispersions provide an additional observational constraint to resolve these processes. We demonstrate this with Figure 5, which shows two successive orbits near the noon-midnight plane. During the first orbit, MESSENGER observed an inflated dayside magnetosphere crossing both the magnetopause and bow shock in the southern hemisphere at distances of 1.83 R_M and 2.77 R_M, respectively. During its dayside traversal, it recorded an energy-dispersed cusp, an equatorial high-energy proton population, and consistent $+B_z$ dominating the interplanetary magnetic field (IMF) in both the magnetosheath and upstream solar wind. Compared to the first orbit, the second was substantially compressed. The bow shock migrated planetward to 1.81 R_M, that is, nearly the location of the magnetopause during the first orbit. Similarly, the magnetopause was observed much closer to the planet too with the spacecraft crossing it at 1.31 R_M. The magnetosheath in the second orbit saw higher proton fluxes and temperatures, was largely dominated by $-B_z$, and had a greater average field strength (119 nT) than the previous orbit (53 nT). These conditions are favorable for intense magnetopause reconnection (e.g., Jasinski, Slavin, et al., 2017). Indeed, signatures of this reconnection can be seen just inside the magnetopause as the spacecraft observed a series of flux ropes and their associated traveling compression regions (e.g., Liu et al., 2008) marked by red ticks.

Despite these differences in the magnetopause and magnetosheath, cusp observations show less change between the two orbits. The second cusp spans greater range in latitude and possesses higher proton flux than the first but both have similar equatorward boundaries ($\Lambda_{cusp} = 62.1 \pm 0.4°$ in the first orbit and $61.7 \pm 0.4°$ in the second) as well as similar dispersions. Fitting these dispersions, the open-closed boundary latitudes are $\Lambda_0 = 58.3 \pm 1.1°$ and

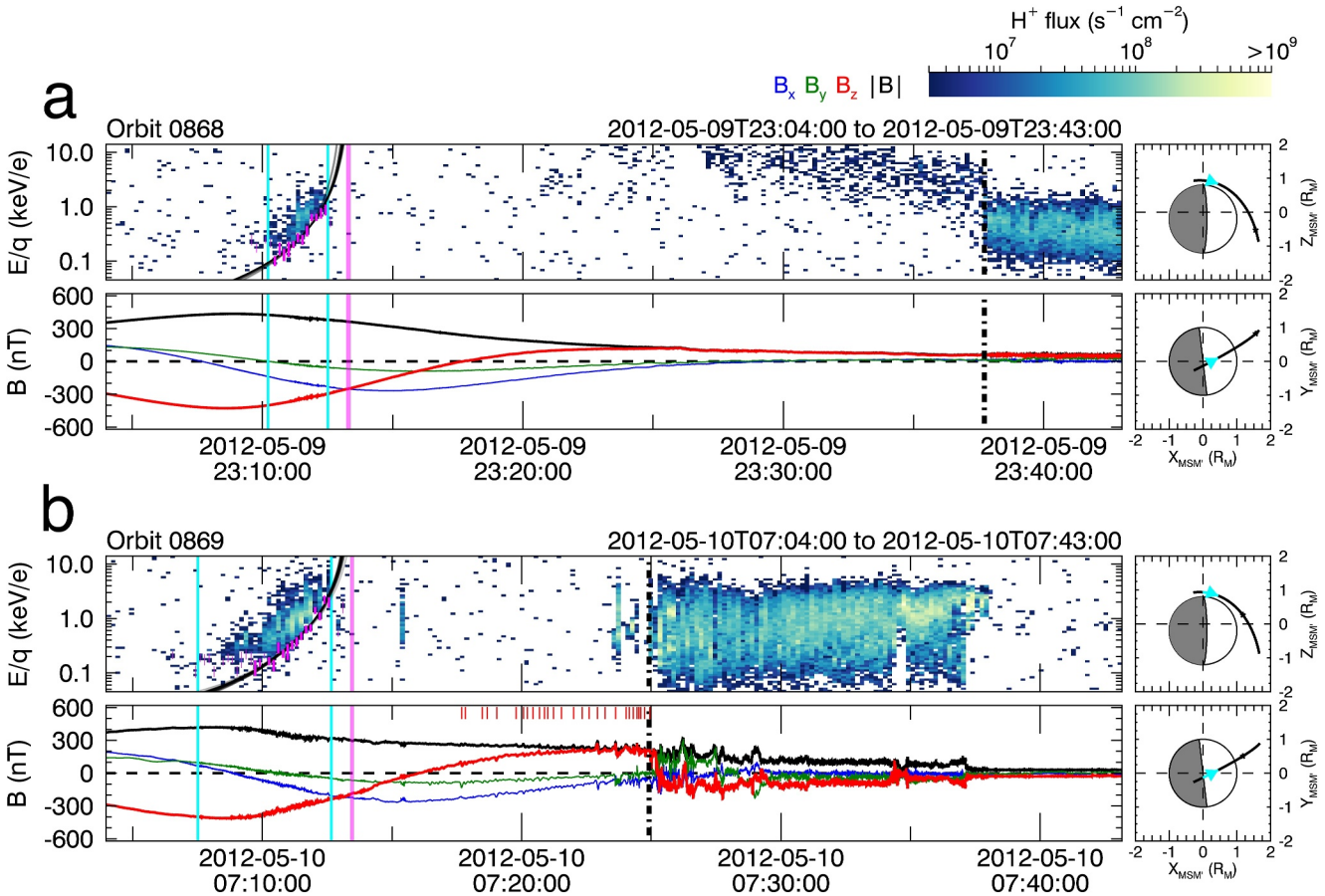


Figure 5. MESSENGER observations from two sequential orbits covering the same portion of the spacecraft's trajectory (i.e., features can be compared directly between the plots). (a) Orbit number 868 and (b) orbit number 869. These orbit observations are in the same general format as in Figure 1 with the addition of dispersion fit features. Similar to Figure 4c, a random subsample of fits is shown as transparent black lines, magenta bars mark $\overline{E}_{\min} \pm \delta\overline{E}_{\min}$ and are scaled by their relative use in the fits, and the vertical magenta line marks the extrapolated crossing of the open-closed boundary. The red ticks in (b) mark flux transfer events. Proton fluxes are in differential energy flux units.

$58.0 \pm 1.0°$, respectively, and $S_0 u_\chi = -38.6 \pm 5.7\,\mathrm{R_M}$ km/s and $-51.4 \pm 5.4\,\mathrm{R_M}$ km/s. Unfortunately, FIPS u_χ flows cannot be confidently resolved for these orbits so we cannot separate u_χ from S_0. However, we expect S_0 to be smaller during the second orbit given the smaller magnetopause standoff distance. Even if we assume S_0 to be the same, the increase in $S_0 u_\chi$ in the second orbit suggests a ~33% increase in the convection speed of magnetic flux to the magnetotail. Given the smaller magnetosheath size as well as the potential for a shorter streaming distance S_0, the greater latitudinal extent of the second cusp is consistent with a faster convection speed. Furthermore, this increased transport is also consistent with the local reconnection signatures in the second orbit and the stronger magnetosheath field.

We can leverage these dispersions to resolve the contribution of compression versus reconnection in determining the magnetopause location. The relative contribution in reducing the magnetopause height in Figure 5b is unclear from the magnetopause crossing alone. While compression will necessarily move the magnetopause planetward, the reconnections signatures about the magnetopause indicate erosion may also play a role. For magnetic reconnection to erode the dayside magnetosphere, it must transport more flux to the magnetotail than the magnetotail returns to the dayside. Consequently, the dayside open-closed boundary will migrate to lower latitudes. Conversely, compression will not change field line topology so it will not change Λ_0. The dispersion fitting resolved that the open-closed boundary location changed negligibly between the two orbits. This indicates that erosion did not contribute to the reduction in magnetopause height between the two orbits and implies that the transition to the lower magnetopause height occurred under balanced nightside and dayside reconnection rates. The

cusp dispersions therefore highlight that the structure of the dayside magnetosphere (e.g., magnetopause standoff distance) can be decoupled from the dayside reconnection rate.

3.2. Probing Mercury's Solar Wind Coupling

In addition to separating the influence of magnetic reconnection from compression in shaping the dayside magnetosphere, cusp dispersions can also be used to more generally probe Mercury's coupling with the solar wind. Figure 6 shows another sequence of noon-midnight orbits where again we can capitalize on the similarity of the orbit to directly compare the time series. Similar to Figure 5, these orbits show variations in the cusp latitude, magnetopause distance, and magnetosheath characteristics, albeit to a less extreme degree. Fitting the energy dispersions within each of the cusps reveals further differences between the orbits. For each of these orbits, FIPS convective u_χ flows can be constrained to within moderate confidence. This allows for determination of S_0 as well as estimating the convective electric field E_ψ by combining the flow with magnetic field observations (i.e., $\tilde{B}$) within the cusp. From these four orbits, we observe some expected correlations. The strongest convective electric field (orbit 1676) is associated with the fastest convective flows, the lowest open-closed boundary, as well as the most intense $-B_z$ and strongest |B| in the magnetosheath. This agrees well with inferences drawn from plasma mantle dispersions at Mercury (Jasinski, Slavin, et al., 2017). However, as examined in Figure 5, this most open magnetosphere does not possess the closest magnetopause, which belongs to the preceding orbit. Furthermore, the last of the four orbits has the second-lowest open-closed boundary latitude despite the greatest magnetopause altitude as well as the most prominent high-energy proton population equatorward of the cusp. This orbit possesses the lowest magnetosheath flux, consistent with a smaller plasma pressure and therefore less compression of the magnetosphere. This orbit series illustrates that cusp dispersions can be correlated with magnetosheath or upstream solar wind parameters to probe Mercury's solar wind coupling. A larger statistical study of MESSENGER cusp observations or with future BepiColombo measurements will be particularly valuable.

3.3. Identifying In Situ Open-Closed Field Line Boundary Crossings

Another compelling feature of this orbit series are the plasma signatures between the cusps and the high-energy protons closer to the magnetopause. Since these orbits are well aligned with the noon-midnight plane we can extrapolate the open-closed boundary crossing to the spacecraft trajectory, as shown in Figure 4c. We show the extrapolated in situ crossings in Figure 6 as highlighted magenta regions and find that each of the orbits contain a proton feature at or near this location. In orbit 1675, the open-closed crossing sits between the high-energy protons and a population of energies (~1–5 keV/e) that lasts a few FIPS scans. This population adjacent to the open-closed boundary is temporally distinct from the cusp and has maximum energies greater than those observed in the cusp or the magnetosheath, but lower average energies than the high-energy population. There is greater uncertainty in orbit 1676, but just poleward of the projected region is a greater concentration of magnetosheath-like protons, including a distinct single FIPS with continuous flux in *E/q*. Equatorward of this population at the upper *E/q* range of the instrument is some evidence of a high-energy proton distribution. Orbit 1677 has a narrow population overlapping with the extrapolated boundary similar to orbit 1675, while the orbit 1678 region bounds a scattered higher energy population continuous from the cusp. While these signatures deserve dedicated future study, they already highlight that in situ signatures of the open-closed boundary may commonly be present within MESSENGER observations and that these signatures may express a range of morphologies. Time-varying magnetosphere conditions could also contribute to these signatures (see Section 3.4).

While the orbit series in Figure 6 illustrates how we may identify in situ open-closed boundary crossings from cusp dispersions, we show another type of example in Figure 7: one in which the spacecraft never observed the closed field region. The dayside traversal in orbit 3504 is extreme in many regards: the cusp spans over 20° in magnetic latitude from 57.9° to 81.7° and is associated with strong diamagnetic signatures in the field; the dayside magnetosphere crossing is short, lasting just 2.5 min, during which large-scale FTEs are observed in the field; the planetward edge of the magnetopause is crossed at 48.5° magnetic latitude at a distance of 1.14 R_M from the dipole center; and a large magnetopause boundary layer ~250 km thick separates the $+B_z$ of the magnetosphere from the strong $-B_z$ of the magnetosheath (−150 nT) within which MESSENGER observes the most intense proton flux within the time series and a shower of small FTEs (e.g., Sun, Slavin, Smith, et al., 2020; Slavin et al., 2012). Fitting the cusp dispersion reveals that the short interval between the cusp and the magnetopause is entirely on open field lines. Shown in Figure 7b, at the equatorward edge of the cusp, the field is almost entirely

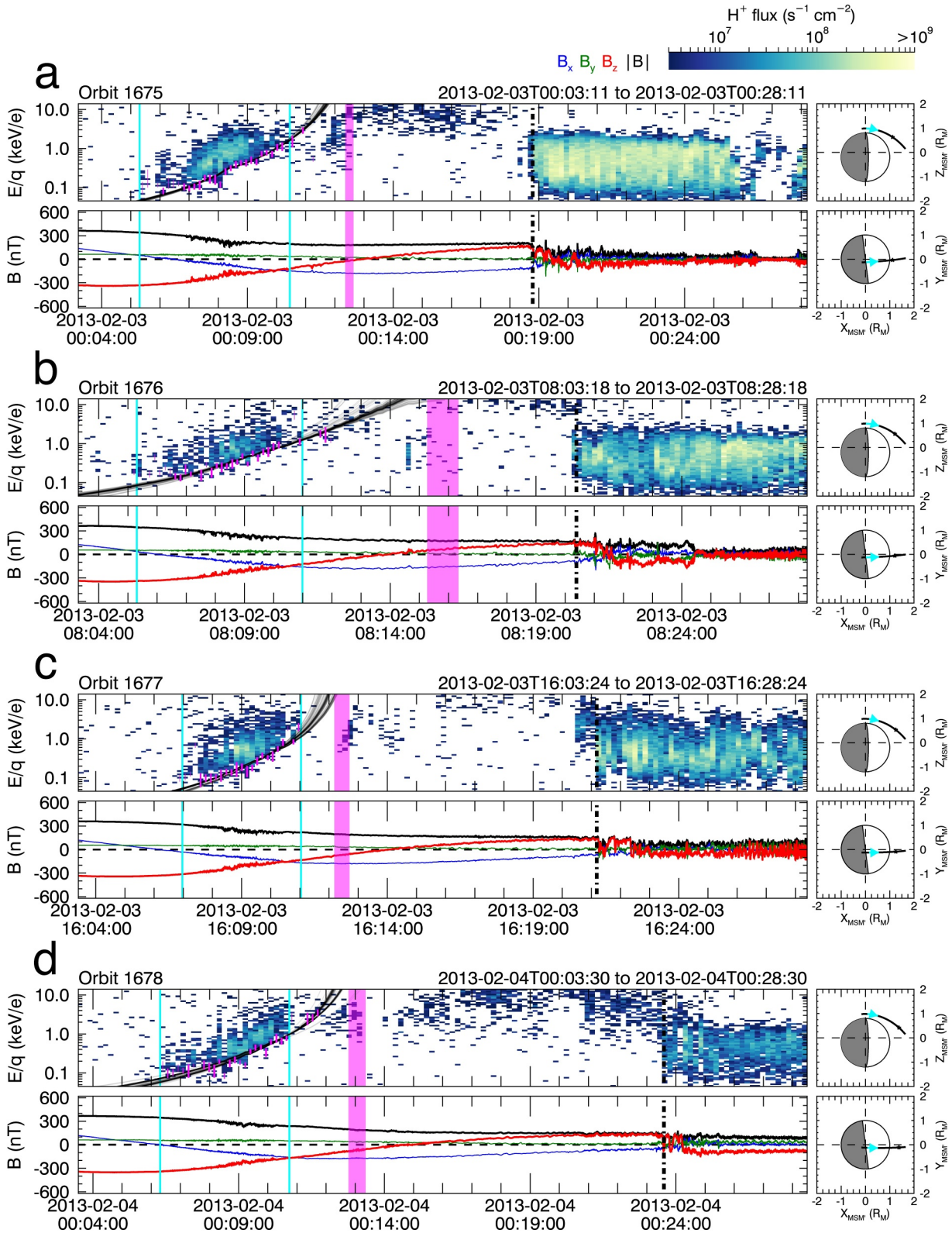


Figure 6. Four sequential orbits in the same format as Figure 5.

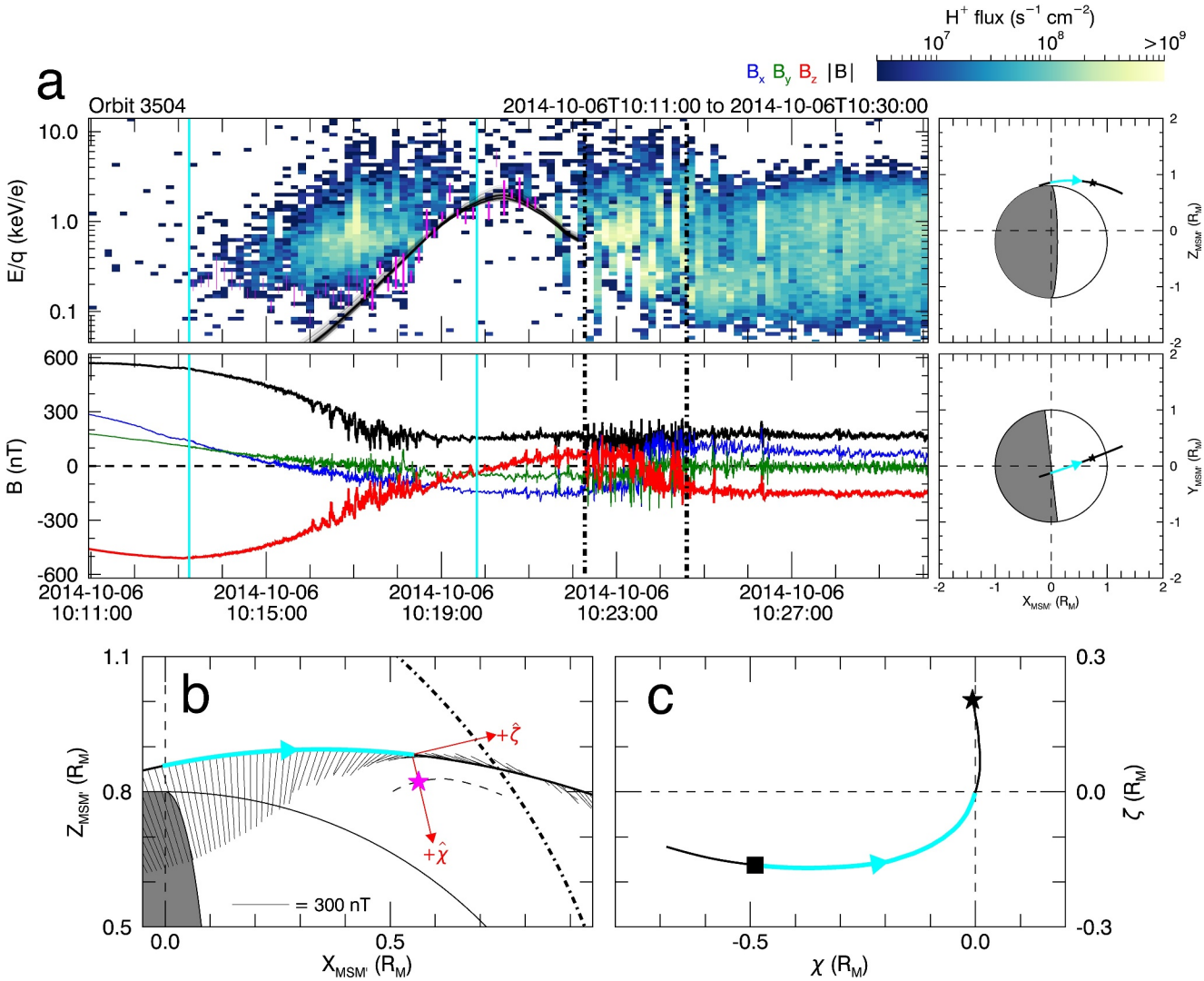


Figure 7. (a) MESSENGER dayside observations in the same format as Figure 5. The two dashed-dotted lines mark the magnetopause boundary layer. (b) Spacecraft trajectory in X-$Z_{MSM'}$ coordinates similar to Figure 2a. The magenta star marks the projected χ_0 location at $\zeta = 0$ and the curved dashed line traces the field line geometry inferred from observations at the spacecraft. (c) Spacecraft trajectory in χ-ζ coordinates similar to Figure 2c, where the black square marks the terminator crossing and the black star the planetmost magnetopause crossing.

horizontal so $+\hat{\chi}$ points primarily toward $-\hat{Z}_{MSM'}$ placing the open-closed boundary 0.062 ± 0.019 R_M below the spacecraft. From the geometry of the observed dayside field lines, an inferred open-closed field line (dashed) maps to below the spacecraft's magnetopause crossing. The implications of this mapping are that the spacecraft remained on open fields through the magnetopause crossing and that the reconnection site was located at lower latitudes. Indeed, the other dispersion parameters support this interpretation. The field line length to the reconnection site is $S_0 = 0.64 \pm 0.26$ R_M. While this value has a fair degree of uncertainty, it confidently places the reconnection site beyond the absolute distance from the cusp to the magnetopause crossing (0.21 R_M). Additionally, the dispersion model in Figure 7a predicts a turning of the observed minimum energy as the spacecraft travels nearly parallel to the field on its way to the magnetopause (see Figure 7c). This trend is observed in the plasma between 10:20:00–10:22:00 and supports this dispersion interpretation.

This example is important as it helps complete the range of dayside magnetosphere topologies encountered by MESSENGER. "Disappearing dayside magnetopause" (DDM) events are the most extreme class of dayside magnetospheres to date (Slavin et al., 2019). These events are identified by the spacecraft crossing the magnetopause at high latitudes into an open $-B_z$ planetary field. In contrast, typical dayside topologies are like those in

Figures 5 and 6 in which the spacecraft crosses the (usually low latitude) magnetopause into the closed $+B_z$ planetary field. The example in Figure 7 illustrates the intermediate case, one in which the spacecraft crosses the magnetopause into an open $+B_z$ planetary field. This type of crossing is perhaps the most difficult to identify because without the aid of a signature to determine field topology (e.g., the cusp dispersion in this example) the $+B_z$ field planetward of the magnetopause would be interpreted as closed field lines.

Finally, as indicated in Table 1, one of the consistent implications of these "classic" energy dispersions (decreasing energy with increasing latitude) is that the cusp is typically poleward of the open-closed boundary. During some orbits (e.g., orbits 665 and 3618), the difference can be on the order of ∼2° while in others, given the rapid convection in Mercury's magnetosphere and the possibility for reconnection to occur at nearly any location on the dayside magnetopause (e.g., Leyser et al., 2017; Zomerdijk-Russell et al., 2023), the cusp can be situated substantially poleward of the open-closed boundary (e.g., orbits 2457 and 1676). From the example dispersions in this paper, the cusp is usually $\Delta\Lambda = 6 \pm 3°$ poleward of the open-closed boundary. At Earth, the stronger planetary magnetic field and weaker IMF result in slower convection at low altitudes such that the cusp is often interpreted to be the equatorward edge of the magnetosphere's polar cap (e.g., Toledo-Redondo et al., 2021). Cusp dispersions at Mercury reveal a greater separation between the polar cap boundary and the cusp location. Estimating the flux budget of the system should be cautious if using the equatorward edge of the cusp as the open-closed boundary. "Reverse" dispersions imply that the open-closed boundary is located poleward of the cusp; their occurrence deserves dedicated study at Mercury.

3.4. Steady-State Magnetosphere

An important component of this framework for analyzing cusp dispersions is the interpretation that they reflect a time-stationary or an approximately steady state of the magnetosphere. While this is a common assumption and has been previously employed in analyzing other dispersions at Mercury (e.g., DiBraccio et al., 2015; Jasinski, Slavin, et al., 2017), it is important to justify its use here. In this interpretation, the dispersion is a fundamentally spatial structure in the cusp that the spacecraft observes as it passes through the region. The duration of the cusp crossing and the dispersion within it are determined by the spacecraft's trajectory through the region. Although we used a single field line to motivate the Section 2.2 conceptual model, in reality, the dispersion signature measured by the spacecraft is the aggregate of many flux tubes. If we consider a flux tube to be defined in radius by the average proton gyroradius (r_c) (i.e., the magnetic field needs to be uniform over this scale for protons to remain associated with these field lines), then the time MESSENGER is connected to an individual flux tube is $2r_c/|u_\chi - u_{sc}| \approx 0.7$ s for cusp $B \sim 250$ nT, $E_\perp \sim 0.5$ keV, $u_\chi \sim 40$ km/s, and the spacecraft's typical speed $u_{sc} \sim 2$ km/s. This estimate is the same duration of FTEs as they pass over the spacecraft (0.5–1 s; Sun, Slavin, Smith, et al., 2020), validating it. FIPS, with a scan time of 10 s, is unable to resolve an individual flux tube as it convects rapidly over the spacecraft. With an average cusp crossing duration of 3.5 min (Raines et al., 2022), MESSENGER encounters hundreds of flux tubes as it passes through the region. To measure a coherent energy dispersion, each of these flux tubes must express the same or similar time-of-flight effect, requiring dayside magnetosphere conditions to remain relatively stable over this period.

If the measured dispersions were purely temporal, then they would require MESSENGER to be connected to the same flux tube throughout its cusp crossing. This would allow dayside conditions to change but be unnoticed by the spacecraft in the cusp. However, this situation is unphysical. If the convection speed were to match the spacecraft speed, then the inferred reconnection sites would be 10s of R_M from the cusp (see $S_0 u_\chi$ in Table 1), well outside of the physical system. Furthermore, this would limit "classic" dispersions to only be observed when the spacecraft is traveling in the same direction as convection, that is, dayside to nightside. In reality, classic dispersions are seen both when MESSENGER travels from nightside to dayside and vice versa, as shown in Figure 1.

In situ observations of the dispersions also support the interpretation of them as spatial structures. As shown in Figure 1, dispersions are observed at all different local times through the cusp, over a range of altitudes, throughout the mission, and both when MESSENGER is traveling from the nightside to the dayside and the opposite. That the spacecraft observes these dispersions in the cusp regardless of its trajectory through the region indicates that these signatures are spatial structures. Furthermore, the detailed analysis of orbit 1915 (Figures 1c, 2, and 4) supports the time-stationary interpretation as the projected open-closed boundary, edge of the high-energy equatorial proton population, and projected magnetopause all coincide. If dayside conditions or the

state of the magnetosphere changed substantially within those ∼15 min then we would not expect these three signatures to align.

While dispersions reflect spatial structures, that does not exclude time variability. Indeed, orbit-to-orbit variations in the cusp flux, magnetic latitude, and dispersion signatures are evident in Figures 5 and 6. Individual cusp crossings, such as orbit 1915, also exhibit scan-to-scan fluctuations. With FIPS's time resolution and counting statistics, it is difficult to tell if these scan-to-scan changes reflect stochastic change (e.g., Poisson statistics) or some variation in the system. In the latter case, the variation is sufficiently small to still produce these large-scale, coherent dispersions. In other words, these dispersions capture the underlying average state of the magnetosphere. In the case of orbit 1915 in particular, multiple magnetopause crossings are observed in quick succession between 00:44 and 00:45 in Figure 1c. For such consistency in the mapped boundaries between 00:29–00:44, this magnetopause motion either had a negligible effect on the dayside magnetosphere structure and reconnection or only began after MESSENGER crossed the magnetopause. During each of the magnetosheath crossings, the direction and strength of the magnetosheath field remain consistent. This supports the interpretation that although the magnetopause was moving periodically, the reconnection site(s) on it likely remained at the same location. Future studies, particularly with numerical modeling of the system, can better constrain the sensitivity of cusp dispersions to changes in magnetopause location or magnetosheath conditions. Additionally, dual spacecraft observations can resolve the spatial versus temporal nature of these cusp dispersions. The TRACERS mission at Earth, for example, will use two identical spacecraft passing through the cusp at slightly different times to resolve spatial versus temporal characteristics (e.g., Trattner et al., 2025). Similar measurements at Mercury, possibly with BepiColombo, will allow for the spatial nature of Mercury's cusp dispersions to be directly tested. Even if TRACERS-like analysis is not feasible with BepiColombo, its faster ion measurement cadence (e.g., 1–4 s for Mio/MPPE-MIA; Saito et al., 2010) will be able to resolve spatiotemporal cusp features and variability that FIPS is not sensitive to.

The steady-state nature of dispersions implies a few characteristics of Mercury's magnetosphere. Foremost, these dispersions highlight that Mercury's magnetosphere can often exhibit steady-state or approximately steady conditions for longer than a Dungey cycle. In the case of orbit 1915, the cusp dispersion, high-energy dayside proton population, and magnetopause location indicate that the magnetosphere was steady for ∼15 min, which is ∼five to eight times the typical Dungey cycle duration (e.g., Imber & Slavin, 2017; Slavin, Anderson, et al., 2010). At a minimum, these dispersions indicate steadiness for at least as long as the cusp crossing, which ranges from 1.6 to 10.3 min in Table 1. While these durations are constrained by MESSENGER's transit time through the cusp, they correspond well to timescales at Mercury's orbit for which the IMF is steady. James et al. (2017) found that over timescales <20 min the IMF typically changes by <2–4 nT. Next, observations of steady magnetospheric convection have been reported at Mercury but during intervals of extreme solar wind driving, including during intense IMF conditions (Sun, Slavin, Dewey, et al., 2020; Zhong, 2024; Zhong et al., 2020, 2023). These cusp dispersions indicate that steady magnetosphere conditions are more common and can occur over a range of IMF and magnetosheath conditions (e.g., Figure 1). Future, more comprehensive studies on the occurrence of cusp dispersions at Mercury can reveal how common the magnetosphere exhibits this time-stationary behavior, for how long, and if it corresponds to steady IMF conditions.

4. Conclusions

In this work, we present the first analysis of energy-latitude dispersions in Mercury's northern magnetospheric cusp. We find that these dispersions are consistent with formation from magnetopause reconnection: the systematic change in observed plasma energy results from time-of-flight effects in particle arrival as the field line convects through the cusp. At Mercury, large-scale coherent dispersions are inherently spatial structures that MESSENGER recorded as it flew through the region.

We fit a model of these dispersions to proton and magnetic field measurements to extract information about the site of magnetopause reconnection and the location of the open-closed field line boundary. Due to the relatively large size of Mercury's northern cusp and MESSENGER's trajectory through it, accounting for spacecraft motion parallel to the magnetic field is required to accurately describe these dispersions. To account for this motion, we transform aberrated Mercury solar magnetospheric coordinates (MSM') into a field-aligned system, which also serves to better resolve perpendicular bulk flows in FIPS observations. Our determination of cusp flows represents the shortest accumulation of FIPS measurements to do so to date, highlighting that FIPS angular

measurements can be used to evaluate flows on $\lesssim$ minute timescales. To support this FIPS analysis, we identify regions of confidence in angular flux maps, greatly expanding previous FIPS techniques. From the FIPS observations, we also evaluated the minimum observed proton energy within each scan. We use an ensemble approach which advances previous methods by quantifying uncertainty. Using the field-coordinate trajectory, bulk flow estimates, and minimum energy measurements, we apply our dispersion model. Similar to determining the minimum energy, we use ensemble and Monte Carlo approaches to evaluate the full uncertainty in the fit. While traditional uncertainties only reflect stochastic sources, this approach captures our uncertainty in the method itself as well. Our careful consideration of uncertainty returns the most robust parameter estimates of the field line length to the reconnection site and the distance to the open-closed boundary.

Applying this framework to "classic" cusp dispersion examples throughout the MESSENGER orbital mission reveals:

1. Mercury's magnetosphere often remains in an approximately steady state for multiple Dungey cycle durations at a time.
2. The cusp does not define the equatorward edge of the polar cap at Mercury; it is usually located poleward of the open-closed boundary by $\sim 6 \pm 3°$ invariant latitude.
3. Cusp dispersions resolve magnetopause reconnection effects (e.g., erosion) from compressive effects in Mercury's dayside magnetosphere.
4. Cusp dispersions can be used to probe Mercury's solar wind coupling.

Future studies can reveal additional features of these cusp dispersions and refine their implications for the magnetosphere. Determining the occurrence rate of these dispersions, their correlation with upstream solar wind conditions, and other dispersion morphologies (e.g., "reverse" dispersions) will be of particular value. Orbital observations from the BepiColombo mission are also expected to shed additional light on these cusp features: the two spacecrafts can directly correlate the upstream solar wind simultaneously with dispersions in the cusp as well as perform TRACERS-like analysis to resolve spatial versus temporal features. Finally, comparison of cusp dispersions with other planetary magnetospheres, particularly Earth's, will be valuable in further understanding fundamental magnetosphere processes such as solar wind coupling.

Appendix A: Cusp Dispersion Fitting

A1. Estimating E_{min} from FIPS

To fit Mercury's cusp dispersions, we first evaluate the minimum particle energy E_{min} from FIPS observations. Several approaches have been taken to quantify the energy extrema in plasma distributions. To analyze cusp dispersions at Earth, for example, Lockwood and Smith (1992) and more recently da Silva et al. (2022) have used the minimum energy at which the flux is $\geq$10% of the peak flux, while at Saturn, Jasinski et al. (2014, 2016) set E_{min} visually. To study plasma mantle dispersions in Mercury's magnetotail, Jasinski, Slavin, et al. (2017) used the highest energy with signal-to-noise ratio (SNR) $\geq$2 defined by Poisson statistics.

To determine E_{min} within Mercury's cusp, we take an ensemble approach. Each of the methods from the previous works above gives an individual estimate of E_{min}, but these estimates are neither guaranteed to agree nor do they have a measure of uncertainty. By applying each of these techniques we develop a distribution of E_{min} from which a central value ($\overline{E}_{\mathrm{min}}$) and its uncertainty ($\delta\overline{E}_{\mathrm{min}}$) can be derived. For each FIPS scan about a cusp crossing, we determine nine estimates of E_{min} following three different general approaches.

Counting statistics approaches:

We use estimates based on counting statistics to acknowledge that there is uncertainty inherent in particle measurements. Energy steps with a single count may be physical, but the confidence from a Poisson perspective is low. By examining the distribution of counts from both discrete and cumulative lenses, we evaluate the minimum energy at which we have statistical confidence.

- The lowest energy with $\geq$2 counts (i.e., SNR > 1).
- The energy of the third cumulative count.

Visual approaches:

We apply a series of metrics to mimic the by-eye identification of E_{min}. For each scan (i.e., column) in the plasma spectrograms in Figure 1, we aim to separate the plasma distribution from its surrounding whitespace (zero counts). To do this, we consider all series of continuous *E/q* steps within the scan that have one or more counts. In the absence of noise, a well-formed distribution would appear as an uninterrupted series of *E/q* steps bounded by whitespace at the energy extrema where the fluxes fall below the instrument's sensitivity. Incorporating random variation, plasma distributions may not be continuous in *E/q*; there may be breaks in the series due to the Poisson nature of the instrument. Therefore, after identifying every continuous series of *E/q* steps with non-zero counts, we merge series that are sufficiently close to each other in *E/q* (i.e., have sufficiently small whitespace gaps between them). We apply several different iterative merging schemes, as listed below, to account for subjective differences in visual identification. After merging, we select the series with the greatest number of total counts and select the lowest energy in it as the E_{min} estimate.

- Merge series with one or fewer zero-count *E/q* steps between them.
- Merge series with two or fewer zero-count steps between them.
- Merge series if the number of zero-count steps between them is smaller than the length of both series.
- Merge series if the number of zero-count steps between them is smaller than or equal to the length of both series.
- Merge series if the number of zero-count steps between them is smaller than or equal to the length of both series plus one.

Fitting approaches:

Finally, we use two fitting procedures to estimate E_{min}. Although the plasma distribution is not required to have a particular shape in *E/q*, we find that cusp distributions are often well-described by 1D Maxwellians. Therefore, we fit the flux distribution with a Gaussian distribution to estimate the mean ($\bar{v}$) and standard deviation (σ_v) of particle speed and use $E_{min} = \frac{1}{2}m(\bar{v} - 2\sigma_v)^2$. This is similar to the Lockwood and Smith (1992) flux criterion but with a threshold of ~13% peak flux. Fitting the distribution to estimate E_{min} rather than directly applying a peak flux threshold to the FIPS measurements better accommodates the count regime and finite telemetry of the mission.

- Fit a Gaussian distribution without incorporating Poisson uncertainty in flux.
- Fit a Gaussian distribution incorporating Poisson uncertainty.

For each of these estimates, we do not impose pitch angle restrictions on the proton distribution. The reasons for this are severalfold: (a) omnidirectional FIPS data has improved counting statistics over directional data; (b) FIPS pointing did not always allow it to measure ~0° pitch angles in the cusp; (c) to reach these low altitudes these protons originated with small pitch angles in the magnetosheath; and (d) analyzing E_{min} places additional pitch angle and streaming restrictions compared to other energies (see Introduction). To illustrate (c), for the orbit 1915 example (Figures 1c and 2), the average magnetosheath field is 55 nT and the average cusp field strength is 253 nT, so to reach the spacecraft, the protons must have had pitch angles of <28° in the magnetosheath.

These nine estimates define a distribution from which the central $\overline{E}_{min}$ value and its uncertainty $\delta\overline{E}_{min}$ are determined. For both parameters, we consider the statistical independence of each of the estimates. While the three approaches are generally independent of each other, the estimates within an approach are not, so we consider the number of independent samples of a given approach to be equal to the square root of the number of successful estimates of that type. We then calculate $\overline{E}_{min}$ as the weighted mean across the successful estimates where the weight for each estimate is proportional to its approach's number of independent samples. For $\delta\overline{E}_{min}$ we combine in quadrature: the standard deviation across the successful estimates reduced by the square root of the total number of independent samples; the finite *E/q* resolution of the instrument at $\overline{E}_{min}$; and the proximity of $\overline{E}_{min}$ to the closest *E/q* step with non-zero counts. We incorporate additional factors of the *E/q* resolution into the uncertainty in the case where one or more approaches yielded no successful estimates to reflect the lower confidence in these plasma scans.

We demonstrate this ensemble approach to $\overline{E}_{min}$ in Figure 4. Figure 4a depicts FIPS proton flux observations near the cusp of orbit 1915 in the field-aligned coordinate system. The plot spans the terminator crossing (right side) to

the reversal in χ trajectory (left side). In this coordinate system, the time series of MESSENGER observations advances from right to left. In Figure 4b $E_{\min}$ estimates are overlaid on a binary mask of the proton distribution, where gray indicates the locations of observed counts. The value of magenta indicates how many of the individual estimates are at each *E/q* step. Within the cusp, the estimates form a continuous ribbon of decreasing energy at the bottom of the proton distribution. The scatter of these estimates illustrates the subjectivity in selecting a minimum energy and the benefits of an ensemble approach, for example, to quantify an uncertainty. In Figure 4c, the estimates are combined to calculate $\overline{E}_{\min}$ and $\delta\overline{E}_{\min}$ in the scans about the cusp. The vertical magenta bars denote $\overline{E}_{\min} \pm \delta\overline{E}_{\min}$, scaled in thickness by their use in ensemble fitting (see below). Overall, the $\overline{E}_{\min}$ in and about the cusp capture the dispersion well. Scan-to-scan fluctuations tend to be small, often overlapping within 1-sigma uncertainty, with an evident decreasing trend characteristic of the energy dispersion. There are a few visual outliers near the boundaries of the cusp, but these scans are marked by greater uncertainty as the plasma distributions in these scans are not as well resolved (e.g., more and larger zero-count whitespace gaps).

A2. FIPS Convection Speed u_χ

Angular FIPS observations can constrain u_χ when viewing geometry and counting statistics are favorable. Dewey et al. (2018, 2020) established numerical techniques to calculate bulk flows and their uncertainties from FIPS observations. We apply these techniques to cusp observations in a field-aligned coordinate system. Due to obstruction from MESSENGER's sunshade and pointing requirements for the spacecraft, FIPS only directly observed $+\hat{X}_{\mathrm{MSM}'}$ or $-\hat{X}_{\mathrm{MSM}'}$ directions during periods of strong solar wind aberration. As a result, FIPS did not typically observe $\pm\hat{\chi}$ directions. However, this pointing perpendicular to the $\hat{\chi}$-axis usually ensures that coverage in the $+\hat{\chi}$ hemisphere is similar to that in the $-\hat{\chi}$ hemisphere. This incomplete, but balanced, angular distribution allows for subsonic plasma flows to be inferred as asymmetries in flux across it. Figure 4e illustrates this with the angular flux map accumulated from the orbit 1915 cusp crossing. In this example, a clear asymmetry toward $-\hat{\chi}$ is apparent. Observations along $\pm\hat{\zeta}$ indicate that FIPS captured both precipitating and reflected protons despite the exact field-aligned direction ($-\hat{\zeta}$) not being within the field of view. Per the criteria established by Dewey et al. (2020) flows in both $\hat{\chi}$ the $\hat{\zeta}$ directions can be evaluated. With no measurements near $-\hat{\psi}$ (edges of the Mollweide projection), flows in $\hat{\psi}$ cannot be rigorously determined.

To derive u_χ and its uncertainty within a cusp crossing, we first assess the angular coverage of the accumulated distribution and whether it supports flow determination per Dewey et al. (2020). If it does, we then apply the Dewey et al. (2018) flow calculation technique. This technique iteratively updates moments calculated from the partial distribution using a software model of FIPS to evaluate the instrument's response to, and impact on moments from unobserved directions. Stochastic and systematic uncertainties are determined from Monte Carlo methods. Since our application of this technique to cusp crossings involves a fewer number of scans (~5–20) than in these previous applications, we take the additional step of excluding directions of low confidence. Confidence is related to both the number of counts recorded along a particular direction as well as how sampled that direction was by instrument's pixels. The region outlined in red in Figure 4e corresponds to directions with SNR ≥ 1 and $N_{\mathrm{pixels}} \geq 50$. This SNR is defined by Poisson statistics and uses the equivalent uncertainty of one count in *E/q* and direction bins were no counts were recorded. We include a limit on the accumulated number of pixels (N_{pixels}) since N_{pixels} sets the flux sensitivity from converting from discrete counts. At $N_{\mathrm{pixels}} = 50$ adding or removing a pixel changes the calculated flux by only ~2% guaranteeing that the conversion from counts to flux is well resolved. We perturb these thresholds to determine their impact on determining u_χ, and since both SNR and N_{pixels} are correlated with angular resolution, we also vary the resolution of the flux maps. These variations are included in the total uncertainty. Following this procedure, we determine the flows in Figure 4e to be $u_\chi = -53 \pm 14$ km/s and $u_\zeta = 12 \pm 9$ km/s.

A3. Fitting the Energy Dispersion

To fit the dispersion model Equation 3, we combine the spacecraft (χ, ζ) location (Section 2.1), minimum observed proton speed $v_{\min} = \sqrt{2\overline{E}_{\min}/m}$ (Section A1), and when available u_χ from FIPS observations (Section A2). When u_χ is constrained, we use $U \equiv u_\chi$. When u_χ is unconstrained, we use $U = -40 \pm 20$ km/s, estimated from a typical cross-magnetosphere potential drop of ~25 kV (Dewey et al., 2018; DiBraccio

et al., 2015; Jasinski, Slavin, et al., 2017; Slavin et al., 2009), an open polar cap area of ∼1 R_M, and cusp field strength of ∼250 nT. Since these values can be highly variable (e.g., Sun, Dewey, et al., 2022 and references therein) we apply multiple random estimates of U as described below. The final terms in Equation 3 involve the magnetic field. For B, we compute the average magnetic field and its uncertainty within each FIPS scan. For $\tilde{B}$, if u_χ can be constrained by FIPS we use a weighted average of B within the cusp where each scan's weight is proportional to its total counts. If u_χ is unconstrained we use $\tilde{B} = 250$ nT for consistency with U.

The next step in applying the dispersion model is to select FIPS scans for fitting. For each cusp crossing, we initialize the fit with a subset of scans. Since numerical fitting can be skewed by outliers, we identify the scans with a confident $\overline{E}_{\rm min}$ estimation: (a) $\overline{E}_{\rm min}$ and $\delta\overline{E}_{\rm min}$ are both real and finite; (b) the signal-to-noise ratio $\overline{E}_{\rm min}/\delta\overline{E}_{\rm min} > 2$; (c) the number of $E_{\rm min}$ estimates exceeds a threshold $N_{\rm est}$; and (d) the total counts in the scan exceed $N_{\rm cts}$. We use default values of $N_{\rm est} = 7$ and $N_{\rm cts} = 6$ but vary them stochastically to capture our full uncertainty in the fitting as described below. From this subset of scans, we then look for saturation of $\overline{E}_{\rm min}$. There are a few physical and instrumental reasons that $\overline{E}_{\rm min}$ may saturate or plateau within the cusp. For instance, the magnetosheath plasma distribution typically exhibits its own minimum energy (see, e.g., the magnetosheath distributions in Figure 1), so in the absence of deceleration, plasma streaming into the cusp will do so above an absolute minimum energy. If the field line length in the magnetosheath is long and/or if magnetosheath connectivity is favorable to the northern cusp (i.e., $B_x < 0$; e.g., Sarantos et al., 2001; He et al., 2017; Zhong et al., 2024) then this absolute minimum energy may be observed within the cusp, particularly if convection is slow. In other words, if there is sufficient time for plasma of any energy to arrive at low altitudes the minimum energy of the magnetosheath will set a floor on $\overline{E}_{\rm min}$ observed in the cusp. Instrumentally, $\overline{E}_{\rm min}$ may saturate if the distribution falls below the *E/q* stepping or range of the instrument (e.g., in Figure 1c FIPS did not sweep all of its voltages as shown in the dark gray). To identify potential saturation of $\overline{E}_{\rm min}$, we calculate an uncertainty-weighted average $\langle\overline{E}_{\rm min}\rangle$ from the lowest 25th percentile of the scan subset and mark any scans with $\overline{E}_{\rm min} - \langle\overline{E}_{\rm min}\rangle < \delta\overline{E}_{\rm min}$ as being potentially saturated. To remove false positives, we then unmark scans if the majority of its four nearest neighbors are unsaturated. The unsaturated scans from the subset are then used for an initial fit.

We use the unsaturated scans from the initial selection to begin a fit of Equation 3. For consistency across dispersions, we fit χ_0 and S_0u_χ as free parameters regardless of whether u_χ can be constrained by FIPS. To filter outliers, to include scans that may have been falsely rejected during selection and/or saturation, and to recognize that the identified cusp boundaries may not be perfect, we iteratively update the fit by removing scans that fall $> \Sigma_1$ from the fit line and introducing scans that fall within $< \Sigma_2$ of it. We use $\Sigma_1 = 5$ and $\Sigma_2 = 2$ by default, where Σ is the minimum distance to the fit line in units of uncertainty. These values reflect that we want it to be relatively difficult to exclude scans but easy to include additional ones. For scans outside of the identified cusp crossing, we limit those that can be introduced by requiring: $N_{\rm est} \geq 6$; $N_{\rm cts} \geq 3$; $\overline{E}_{\rm min}/\delta\overline{E}_{\rm min} \geq 2$; $|t_{\rm scan} - t_{\rm cusp}| < 1$ min; and $\Delta\chi\Delta X_{\rm MSM'} \geq 0$. These criteria help to ensure that a plasma distribution is present and that potentially closed field lines closer to the magnetopause are avoided. We propagate uncertainties associated with each of the terms used in the fit. To complement these uncertainties, we perform a subsample analysis once the scans used in the fit have converged. We select half of the final scans at random without replacement and fit them, then repeat this process 100 times to develop a distribution of solutions and their corresponding errors.

The final component to our fitting procedure is to develop probability distributions for χ_0 and S_0 (or S_0u_χ) by varying the threshold values above according to a Monte Carlo procedure. We vary $N_{\rm est}$, $N_{\rm cts}$, Σ_1, Σ_2, and U (if u_χ was not constrained by FIPS). For 1,000 iterations of the above procedure, we select values at random according to the following distributions: $N_{\rm est} \sim G(7,1)$, $N_{\rm cts} \sim P(6)$, $\Sigma_1 \sim G(5,1)$, $\Sigma_2 \sim G(2,1)$, and $U \sim G(-40,20)$ where $P(\lambda)$ is a Poisson distribution of mean λ and $G(\mu,\sigma)$ is a Gaussian distribution of mean μ and standard deviation σ. We limit $N_{\rm est} \leq 9$, $N_{\rm cts} \geq 1$, $\Sigma_1 \geq 1$, and $\Sigma_2 \leq 3$ to avoid unphysical results. We use the resulting 100,000 individual subsample fits to construct a joint probability distribution for χ_0 and S_0u_χ. Our use of ensemble techniques, iteration, and randomization provides the most robust estimates of these parameters by evaluating and propagating uncertainties not only related to the instrument but those related to the method itself.

We illustrate this fitting procedure in Figure 4. In Figure 4c, the vertical magenta bars indicate $\overline{E}_{\rm min} \pm \delta\overline{E}_{\rm min}$ for the scans about the cusp available for fitting. The thickness of these bars scales with their relative use in the ensemble of fits, which are shown as thin transparent black curves. Visually, these fits match the dispersion well

and involve the majority of the cusp. Within the cusp, 14 of the 24 scans are selected in nearly every scan subset (i.e., are selected for nearly half of all subsample fits). Of the scans that are not regularly involved in the fitting, one is a high energy outlier near $\chi \sim 0.02$ R_M and several are at the poleward edge of the cusp and identified as scans following $\overline{E}_{min}$ saturation. Outside of the cusp, a few scans adjacent to each of the cusp boundaries are available for the fitting procedure; however, only the two scans just equatorward of the cusp were selected for fitting. Due to the variation in thresholds from the Monte Carlo procedure, there is some difference in the individual fits. Within the center of the cusp at $\chi \sim -0.07$ to -0.22 R_M differences between individual fits are on the order of the average $\delta\overline{E}_{min}$, but projected equatorward of the cusp, these differences are more pronounced. This highlights the value of a large range in $\overline{E}_{min}$ in constraining a dispersion. In this example, of the commonly fit scans, $\overline{E}_{min}$ spans an order of magnitude from 0.13 to 1.53 keV/e.

The effect of the spread in individual fits can be seen in Figure 4d, the marginal probability distribution of χ_0. Here, we show the effects of using a random U (red) versus $U \equiv u_\chi$ constrained by FIPS (gray distribution). Both distributions are approximately Gaussian with a small skew toward lower χ. Use of the more accurate u_χ shifts the distribution slightly but has a larger effect in narrowing the width. Using random U, $\chi_0 = 0.096 \pm 0.016$ R_M and $S_0u_\chi = -45.5 \pm 5.7$ R_M km/s compared to $\chi_0 = 0.092 \pm 0.013$ R_M and $S_0u_\chi = -44.4 \pm 4.0$ R_M km/s for $U \equiv u_\chi$. The more accurate and more precise $U \equiv u_\chi$ has a greater effect on reducing both parameters' uncertainty (~20% reduction) than on the central value. This highlights how χ_0 and S_0u_χ can still be reliably inferred from dispersions without precise knowledge of u_χ.

Data Availability Statement

All MESSENGER data used in this study are available from the Planetary Plasma Interactions node of the NASA Planetary Data System (https://pds-ppi.igpp.ucla.edu/).

Acknowledgments
This work was supported by NASA Planetary Science Division Grant 80NSSC24K0059. JAS acknowledges support provided by NASA Planetary Science Division Grant 80NSSC21K0052. JMJ acknowledges support from the Jet Propulsion Laboratory, California Institute of Technology, under NASA contract 80NM0018D0004.

References

Anderson, B. J., Acuña, M. H., Lohr, D. A., Scheifele, J., Raval, A., Korth, H., & Slavin, J. A. (2007). The magnetometer instrument on MESSENGER. *Space Science Reviews*, *131*(1–4), 417–450. https://doi.org/10.1007/s11214-007-9246-7

Anderson, B. J., Johnson, C. L., Korth, H., Purucker, M. E., Winslow, R. M., Slavin, J. A., et al. (2011). The global magnetic field of Mercury from MESSENGER orbital observations. *Science (New York, N.Y.)*, *333*(6051), 1859–1862. https://doi.org/10.1126/science.1211001

Andrews, G. B., Zurbuchen, T. H., Mauk, B. H., Malcom, H., Fisk, L. A., Gloeckler, G., et al. (2007). The energetic particle and plasma spectrometer instrument on the MESSENGER spacecraft. *Space Science Reviews*, *131*(1–4), 523–556. https://doi.org/10.1007/s11214-007-9272-5

Arridge, C. S., Jasinski, J. M., Achilleos, N., Bogdanova, Y. V., Bunce, E. J., Cowley, S. W. H., et al. (2016). Cassini observations of Saturn's southern polar cusp. *Journal of Geophysical Research: Space Physics*, *121*(4), 3006–3030. https://doi.org/10.1002/2015ja021957

Brain, D. A., Bagenal, F., Acuña, M. H., & Connerney, J. E. P. (2003). Martian magnetic morphology: Contributions from the solar wind and crust. *Journal of Geophysical Research*, *108*(A12), 1424. https://doi.org/10.1029/2002ja009482

Burch, J. L., Reiff, P. H., Heelis, R. A., Winningham, J. D., Hanson, W. B., Gurgiolo, C., et al. (1982). Plasma injection and transport in the mid-altitude polar cusp. *Geophysical Research Letters*, *9*, 921–924. https://doi.org/10.1029/GL009i009p00921

Chen, Y., Tóth, G., Jia, X., Slavin, J. A., Sun, W., Markidis, S., et al. (2019). Studying dawn-dusk asymmetries of Mercury's magnetotail using MHD-EPIC simulations. *Journal of Geophysical Research: Space Physics*, *124*(11), 8954–8973. https://doi.org/10.1029/2019ja026840

Collinson, G., Paterson, W. R., Bard, C., Dorelli, J., Glocer, A., Sarantos, M., & Wilson, R. (2018). New results from *Galileo*'s first flyby of Ganymede: Reconnection-driven flows at the Low-latitude magnetopause boundary, crossing the cusp, and icy ionospheric escape. *Geophysical Research Letters*, *45*(8), 3382–3392. https://doi.org/10.1002/2017gl075487

Connor, H. K., Raeder, J., Sibeck, D. G., & Trattner, K. J. (2015). Relation between cusp ion structures and dayside reconnection for four IMF clock angles: OpenGGCM-LTPT results. *Journal of Geophysical Research: Space Physics*, *120*(6), 4890–4906. https://doi.org/10.1002/2015ja021156

da Silva, D., Chen, L. J., Fuselier, S., Wang, S., Elkington, S., Dorelli, J., et al. (2022). Automatic identification and new observations of ion energy dispersion events in the cusp ionosphere. *Journal of Geophysical Research: Space Physics*, *127*(4), e2021JA029637. https://doi.org/10.1029/2021ja029637

Dewey, R. M., Raines, J. M., Sun, W., Slavin, J. A., & Poh, G. (2018). MESSENGER observations of fast plasma flows in Mercury's magnetotail. *Geophysical Research Letters*, *45*(19), 10110–10118. https://doi.org/10.1029/2018gl079056

Dewey, R. M., Slavin, J. A., Raines, J. M., Azari, A. R., & Sun, W. (2020). MESSENGER observations of flow braking and flux pileup of dipolarizations in Mercury's magnetotail: Evidence for current wedge formation. *Journal of Geophysical Research: Space Physics*, *125*(9), e2020JA028112. https://doi.org/10.1029/2020ja028112

DiBraccio, G. A., Slavin, J. A., Boardsen, S. A., Anderson, B. J., Korth, H., Zurbuchen, T. H., et al. (2013). MESSENGER observations of magnetopause structure and dynamics at Mercury. *Journal of Geophysical Research: Space Physics*, *118*(3), 997–1008. https://doi.org/10.1002/jgra.50123

DiBraccio, G. A., Slavin, J. A., Raines, J. M., Gershman, D. J., Tracy, P. J., Boardsen, S. A., et al. (2015). First observations of Mercury's plasma mantle by MESSENGER. *Geophysical Research Letters*, *42*(22), 9666–9675. https://doi.org/10.1002/2015gl065805

Exner, W., Heyner, D., Liuzzo, L., Motschmann, U., Shiota, D., Kusano, K., & Shibayama, T. (2018). Coronal mass ejection hits Mercury: A.I.K. E.F. hybrid-code results compared to MESSENGER data. *Planetary and Space Science*, *153*, 89–99. https://doi.org/10.1016/j.pss.2017.12.016

Fatemi, S., Poirier, N., Holmström, M., Lindkvist, J., Wieser, M., & Barabash, S. (2018). A modelling approach to infer the solar wind dynamic pressure from magnetic field observations inside Mercury's magnetosphere. *Astronomy & Astrophysics*, *614*, A132. https://doi.org/10.1051/0004-6361/201832764

Fear, R. C., Coxon, J. C., & Jackman, C. M. (2019). The contribution of flux transfer events to Mercury's dungey cycle. *Geophysical Research Letters*, *46*(24), 14239–14246. https://doi.org/10.1029/2019GL085399

Fuselier, S. A., Kletzing, C. A., Petrinec, S. M., Trattner, K. J., George, D., Bounds, S. R., et al. (2022). Multiple reconnection X-lines at the magnetopause and overlapping cusp ion injections. *Journal of Geophysical Research: Space Physics*, *127*(5), e2022JA030354. https://doi.org/10.1029/2022ja030354

Gershman, D. J., Slavin, J. A., Raines, J. M., Zurbuchen, T. H., Anderson, B. J., Korth, H., et al. (2013). Magnetic flux pileup and plasma depletion in Mercury's subsolar magnetosheath. *Journal of Geophysical Research: Space Physics*, *118*(11), 7181–7199. https://doi.org/10.1002/2013ja019244

Glassmeier, K.-H., Auster, H.-U., & Motschmann, U. (2007). A feedback dynamo generating Mercury's magnetic field. *Geophysical Research Letters*, *34*(22), L22201. https://doi.org/10.1029/2007gl031662

Halekas, J. S., Delory, G. T., Brain, D. A., Lin, R. P., & Mitchell, D. L. (2008). Density cavity observed over a strong lunar crustal magnetic anomaly in the solar wind: A mini-magnetosphere? *Planetary and Space Science*, *56*(7), 941–946. https://doi.org/10.1016/j.pss.2008.01.008

He, M., Vogt, J., Heyner, D., & Zhong, J. (2017). Solar wind controls on Mercury's magnetospheric cusp. *Journal of Geophysical Research: Space Physics*, *122*(6), 6150–6164. https://doi.org/10.1002/2016ja023687

Hood, L. L., & Schubert, G. (1979). Inhibition of solar wind impingement on Mercury by planetary induction currents. *Journal of Geophysical Research*, *84*(A6), 2641–2647. https://doi.org/10.1029/ja084ia06p02641

Imber, S. M., & Slavin, J. A. (2017). MESSENGER observations of magnetotail loading and unloading: Implications for substorms at Mercury. *Journal of Geophysical Research: Space Physics*, *122*(11), 11402–11412. https://doi.org/10.1002/2017ja024332

Imber, S. M., Slavin, J. A., Boardsen, S. A., Anderson, B. J., Korth, H., McNutt, R. L., & Solomon, S. C. (2014). MESSENGER observations of large dayside flux transfer events: Do they drive Mercury's substorm cycle? *Journal of Geophysical Research: Space Physics*, *119*(7), 5613–5623. https://doi.org/10.1002/2014JA019884

James, M. K., Imber, S. M., Bunce, E. J., Yeoman, T. K., Lockwood, M., Owens, M. J., & Slavin, J. A. (2017). Interplanetary magnetic field properties and variability near Mercury's orbit. *Journal of Geophysical Research: Space Physics*, *122*(8), 7907–7924. https://doi.org/10.1002/2017JA024435

Jasinski, J. M., Arridge, C. S., Coates, A. J., Jones, G. H., Sergis, N., Thomsen, M. F., & Krupp, N. (2017). Diamagnetic depression observations at Saturn's magnetospheric cusp by the Cassini spacecraft. *Journal of Geophysical Research: Space Physics*, *122*(6), 6283–6303. https://doi.org/10.1002/2016ja023738

Jasinski, J. M., Arridge, C. S., Coates, A. J., Jones, G. H., Sergis, N., Thomsen, M. F., et al. (2016). Cassini plasma observations of Saturn's magnetospheric cusp. *Journal of Geophysical Research: Space Physics*, *121*(12), 12047–12067. https://doi.org/10.1002/2016ja023310

Jasinski, J. M., Arridge, C. S., Lamy, L., Leisner, J. S., Thomsen, M. F., Mitchell, D. G., et al. (2014). Cusp observation at Saturn's high-latitude magnetosphere by the Cassini spacecraft. *Geophysical Research Letters*, *41*(5), 1382–1388. https://doi.org/10.1002/2014gl059319

Jasinski, J. M., Murphy, N., Jia, X., & Slavin, J. A. (2022). Neptune's pole-on magnetosphere: Dayside reconnection observations by Voyager 2. *Planetary Science Journal J.*, *3*(4), 76. https://doi.org/10.3847/psj/ac5967

Jasinski, J. M., Slavin, J. A., Raines, J. M., & DiBraccio, G. A. (2017). Mercury's solar wind interaction as characterized by magnetospheric plasma mantle observations with MESSENGER. *Journal of Geophysical Research: Space Physics*, *122*(12), 12153–12169. https://doi.org/10.1002/2017ja024594

Jia, X., Slavin, J. A., Gombosi, T. I., Daldorff, L. K. S., Toth, G., & van der Holst, B. (2015). Global MHD simulations of Mercury's magnetosphere with coupled planetary interior: Induction effect of the planetary conducting core on the global interaction. *Journal of Geophysical Research: Space Physics*, *120*(6), 4763–4775. https://doi.org/10.1002/2015ja021143

Jia, X., Slavin, J. A., Poh, G., DiBraccio, G. A., Toth, G., Chen, Y., et al. (2019). MESSENGER observations and global simulations of highly compressed magnetosphere events at Mercury. *Journal of Geophysical Research: Space Physics*, *124*(1), 229–247. https://doi.org/10.1029/2018ja026166

Kivelson, M. G., Khurana, K. K., Coroniti, F. V., Joy, S., Russell, C. T., Walker, R. J., et al. (1997). The magnetic field and magnetosphere of Ganymede. *Geophysical Research Letters*, *24*(17), 2155–2158. https://doi.org/10.1029/97gl02201

Korth, H., Johnson, C. L., Philpott, L., Tsyganenko, N. A., & Anderson, B. J. (2017). A dynamic model of Mercury's magnetospheric magnetic field. *Geophysical Research Letters*, *44*(20), 10147–10154. https://doi.org/10.1002/2017gl074699

Lamy, L., Prangé, R., Tao, C., Kim, T., Badman, S. V., Zarka, P., et al. (2018). Saturn's northern aurorae at solstice from HST observations coordinated with Cassini's grand finale. *Geophysical Research Letters*, *45*(18), 9353–9362. https://doi.org/10.1029/2018gl078211

Lavraud, B., & Trattner, K. J. (2021). The polar cusps of the earth's magnetosphere. In *Geophysical monograph series* (pp. 163–176). Wiley. https://doi.org/10.1002/9781119815624.ch11

Lepping, R. P., Burlaga, L. F., Lazarus, A. J., Vasyliunas, V. M., Szabo, A., Steinberg, J., et al. (1992). Neptune's polar cusp region: Observations and magnetic field analysis. *Journal of Geophysical Research*, *97*(A6), 8135–8144. https://doi.org/10.1029/92JA00314

Leyser, R. P., Imber, S. M., Milan, S. E., & Slavin, J. A. (2017). The influence of IMF clock angle on dayside flux transfer events at Mercury. *Geophysical Research Letters*, *44*(21), 10829–10837. https://doi.org/10.1002/2017gl074858

Li, C., Jia, X., Chen, Y., Toth, G., Zhou, H., Slavin, J. A., et al. (2024). Kinetic signatures, dawn-dusk asymmetries, and flux transfer events associated with Mercury's dayside magnetopause reconnection from 3D MHD-AEPIC simulations. *Journal of Geophysical Research: Space Physics*, *129*(6), e2024JA032669. https://doi.org/10.1029/2024ja032669

Liu, J., Angelopoulos, V., Sibeck, D., Phan, T., Pu, Z. Y., McFadden, J., et al. (2008). THEMIS observations of the dayside traveling compression region and flows surrounding flux transfer events. *Geophysical Research Letters*, *35*(17), L17S07. https://doi.org/10.1029/2008gl033673

Lockwood, M. (1995). Location and characteristics of the reconnection X line deduced from low-altitude satellite and ground-based observations: 1. Theory. *Journal of Geophysical Research*, *100*(A11), 21791–21802. https://doi.org/10.1029/95ja01340

Lockwood, M., Davis, C. J., Smith, M. F., Onsager, T. G., & Denig, W. F. (1995). Location and characteristics of the reconnection X line deduced from low-altitude satellite and ground-based observations: 2. Defense meteorological satellite program and European incoherent scatter data. *Journal of Geophysical Research*, *100*(A11), 21803–21813. https://doi.org/10.1029/95ja01339

Lockwood, M., Onsager, T. G., Davis, C. J., Smith, M. F., & Denig, W. F. (1994). The characteristics of the magnetopause reconnection X-line deduced from low-altitude satellite observations of cusp ions. *Geophysical Research Letters*, *21*(24), 2757–2760. https://doi.org/10.1029/94gl02696

Lockwood, M., & Smith, M. F. (1989). Low-altitude signatures of the cusp and flux transfer events. *Geophysical Research Letters*, *16*(8), 879–882. https://doi.org/10.1029/gl016i008p00879

Lockwood, M., & Smith, M. F. (1992). The variation of reconnection rate at the dayside magnetopause and cusp ion precipitation. *Journal of Geophysical Research*, *97*(A10), 14841–14847. https://doi.org/10.1029/92ja01261

Mangano, V., Massetti, S., Milillo, A., Plainaki, C., Orsini, S., Rispoli, R., & Leblanc, F. (2015). THEMIS Na exosphere observations of Mercury and their correlation with in-situ magnetic field measurements by MESSENGER. *Planetary and Space Science*, *115*, 102–109. https://doi.org/10.1016/j.pss.2015.04.001

Paty, C., & Winglee, R. (2004). Multi-fluid simulations of Ganymede's magnetosphere. *Geophysical Research Letters*, *31*(24), L24806. https://doi.org/10.1029/2004gl021220

Philpott, L. C., Johnson, C. L., Anderson, B. J., & Winslow, R. M. (2020). The shape of Mercury's magnetopause: The picture from MESSENGER magnetometer observations and future prospects for BepiColombo. *Journal of Geophysical Research: Space Physics*, *125*(5), e2019JA027544. https://doi.org/10.1029/2019ja027544

Pitout, F., & Bogdanova, Y. V. (2021). The polar cusp seen by Cluster. *Journal of Geophysical Research: Space Physics*, *126*(9), e2021JA029582. https://doi.org/10.1029/2021ja029582

Poh, G., Slavin, J. A., Jia, X., DiBraccio, G. A., Raines, J. M., Imber, S. M., et al. (2016). MESSENGER observations of cusp plasma filaments at Mercury. *Journal of Geophysical Research: Space Physics*, *121*(9), 8260–8285. https://doi.org/10.1002/2016ja022552

Poppe, A. R., Brain, D. A., Dong, Y., Xu, S., & Jarvinen, R. (2021). Particle-in-cell modeling of Martian magnetic cusps and their role in enhancing nightside ionospheric ion escape. *Geophysical Research Letters*, *48*(1), e2020GL090763. https://doi.org/10.1029/2020gl090763

Poppe, A. R., Halekas, J. S., Delory, G. T., & Farrell, W. M. (2012). Particle-in-cell simulations of the solar wind interaction with lunar crustal magnetic anomalies: Magnetic cusp regions. *Journal of Geophysical Research*, *117*(A9), A09105. https://doi.org/10.1029/2012ja017844

Pump, K., Heyner, D., Schmid, D., Exner, W., & Plaschke, F. (2024). Revised magnetospheric model reveals signatures of field-aligned current systems at Mercury. *Journal of Geophysical Research: Space Physics*, *129*(3), e2023JA031529. https://doi.org/10.1029/2023ja031529

Raines, J. M., Dewey, R. M., Staudacher, N. M., Tracy, P. J., Bert, C. M., Sarantos, M., et al. (2022). Proton precipitation in Mercury's northern magnetospheric cusp. *Journal of Geophysical Research: Space Physics*, *127*(11), e2022JA030397. https://doi.org/10.1029/2022ja030397

Raines, J. M., Gershman, D. J., Slavin, J. A., Zurbuchen, T. H., Korth, H., Anderson, B. J., & Solomon, S. C. (2014). Structure and dynamics of Mercury's magnetospheric cusp: MESSENGER measurements of protons and planetary ions. *Journal of Geophysical Research: Space Physics*, *119*(8), 6587–6602. https://doi.org/10.1002/2014ja020120

Reiff, P. H., Hill, T. W., & Burch, J. L. (1977). Solar wind plasma injection at the dayside magnetospheric cusp. *Journal of Geophysical Research*, *82*(4), 479–491. https://doi.org/10.1029/ja082i004p00479

Rosenbauer, H., Grünwaldt, H., Montgomery, M. D., Paschmann, G., & Sckopke, N. (1975). HEOS 2 plasma observations in the distant polar magnetosphere: The plasma mantle. *Journal of Geophysical Research*, *80*(19), 2723–2737. https://doi.org/10.1029/ja080i019p02723

Saito, Y., Sauvaud, J. A., Hirahara, M., Barabash, S., Delcourt, D., Takashima, T., et al. (2010). Scientific objectives and instrumentation of Mercury plasma particle experiment (MPPE) onboard MMO. *Planetary and Space Science*, *58*(1–2), 182–200. https://doi.org/10.1016/j.pss.2008.06.003

Sarantos, M., Reiff, P. H., Hill, T. W., Killen, R. M., & Urquhart, A. L. (2001). A B_x-interconnected magnetosphere model for Mercury. *Planetary and Space Science*, *49*(14–15), 1629–1635. https://doi.org/10.1016/s0032-0633(01)00100-3

Slavin, J. A., Acuña, M. H., Anderson, B. J., Baker, D. N., Benna, M., Boardsen, S. A., et al. (2009). MESSENGER observations of magnetic reconnection in Mercury's magnetosphere. *Science (New York, N.Y.)*, *324*(5927), 606–610. https://doi.org/10.1126/science.1172011

Slavin, J. A., Anderson, B. J., Baker, D. N., Benna, M., Boardsen, S. A., Gloeckler, G., et al. (2010). MESSENGER observations of extreme loading and unloading of Mercury's magnetic tail. *Science (New York, N.Y.)*, *329*(5992), 665–668. https://doi.org/10.1126/science.1188067

Slavin, J. A., DiBraccio, G. A., Gershman, D. J., Imber, S. M., Poh, G. K., Raines, J. M., et al. (2014). MESSENGER observations of Mercury's dayside magnetosphere under extreme solar wind conditions. *Journal of Geophysical Research: Space Physics*, *119*(10), 8087–8116. https://doi.org/10.1002/2014ja020319

Slavin, J. A., & Holzer, R. E. (1979). The effect of erosion on the solar wind stand-off distance at Mercury. *Journal of Geophysical Research*, *84*(A5), 2076–2082. https://doi.org/10.1029/ja084ia05p02076

Slavin, J. A., Imber, S. M., Boardsen, S. A., DiBraccio, G. A., Sundberg, T., Sarantos, M., et al. (2012). MESSENGER observations of a flux-transfer-event shower at Mercury. *Journal of Geophysical Research*, *117*(A12), A00M06. https://doi.org/10.1029/2012ja017926

Slavin, J. A., Lepping, R. P., Wu, C.-C., Anderson, B. J., Baker, D. N., Benna, M., et al. (2010). MESSENGER observations of large flux transfer events at Mercury. *Geophysical Research Letters*, *37*(2), L02105. https://doi.org/10.1029/2009GL041485

Slavin, J. A., Middleton, H. R., Raines, J. M., Jia, X., Zhong, J., Sun, W.-J., et al. (2019). MESSENGER observations of disappearing dayside magnetosphere events at Mercury. *Journal of Geophysical Research: Space Physics*, *124*(8), 6613–6635. https://doi.org/10.1029/2019ja026892

Suess, S. T., & Goldstein, B. E. (1979). Compression of the Hermaean magnetosphere by the solar wind. *Journal of Geophysical Research*, *84*(A7), 3306–3312. https://doi.org/10.1029/ja084ia07p03306

Sun, W., Dewey, R. M., Aizawa, S., Huang, J., Slavin, J. A., Fu, S., et al. (2022). Review of Mercury's dynamic magnetosphere: Post-MESSENGER era and comparative magnetospheres. *Science China Earth Sciences*, *65*(1), 25–74. https://doi.org/10.1007/s11430-021-9828-0

Sun, W., Slavin, J. A., Milillo, A., Dewey, R. M., Orsini, S., Jia, X., et al. (2022). MESSENGER observations of planetary ion enhancements at Mercury's northern magnetospheric cusp during flux transfer event showers. *Journal of Geophysical Research: Space Physics*, *127*(4), e2022JA030280. https://doi.org/10.1029/2022ja030280

Sun, W. J., Slavin, J. A., Dewey, R. M., Chen, Y., DiBraccio, G. A., Raines, J. M., et al. (2020). MESSENGER observations of Mercury's nightside magnetosphere under extreme solar wind conditions: Reconnection-generated structures and steady convection. *Journal of Geophysical Research: Space Physics*, *125*(3), e2019JA027490. https://doi.org/10.1029/2019ja027490

Sun, W. J., Slavin, J. A., Smith, A. W., Dewey, R. M., Poh, G. K., Jia, X., et al. (2020). Flux transfer event showers at Mercury: Dependence on plasma β and magnetic shear and their contribution to the dungey cycle. *Geophysical Research Letters*, *47*(21), e2020GL089784. https://doi.org/10.1029/2020gl089784

Toledo-Redondo, S., André, M., Aunai, N., Chappell, C. R., Dargent, J., Fuselier, S. A., et al. (2021). Impacts of ionospheric ions on magnetic reconnection and Earth's magnetosphere dynamics. *Reviews of Geophysics*, *59*(3), e2020RG000707. https://doi.org/10.1029/2020rg000707

Trattner, K. J., LaBelle, J., Santolik, O., Kletzing, C. A., Miles, D. M., Fuselier, S. A., et al. (2025). From the TRICE-2 investigations to the TRACERS mission. *Space Science Reviews*, *221*(4), 52. https://doi.org/10.1007/s11214-025-01178-2

Trattner, K. J., Petrinec, S. M., Fuselier, S. A., Omidi, N., & Sibeck, D. G. (2012). Evidence of multiple reconnection lines at the magnetopause from cusp observations. *Journal of Geophysical Research*, *117*(A1), A01213. https://doi.org/10.1029/2011ja017080

Weber, T., Brain, D., Xu, S., Mitchell, D., Espley, J., Halekas, J., et al. (2020). The influence of interplanetary magnetic field direction on Martian crustal magnetic field topology. *Geophysical Research Letters*, *47*(19), e2020GL087757. https://doi.org/10.1029/2020gl087757

Wieser, M., Barabash, S., Futaana, Y., Holmström, M., Bhardwaj, A., Sridharan, R., et al. (2010). First observation of a mini-magnetosphere above a lunar magnetic anomaly using energetic neutral atoms. *Geophysical Research Letters*, *37*(5), L05103. https://doi.org/10.1029/2009gl041721

Winslow, R. M., Anderson, B. J., Johnson, C. L., Slavin, J. A., Korth, H., Purucker, M. E., et al. (2013). Mercury's magnetopause and bow shock from MESSENGER magnetometer observations. *Journal of Geophysical Research: Space Physics*, *118*(5), 2213–2227. https://doi.org/10.1002/jgra.50237

Winslow, R. M., Johnson, C. L., Anderson, B. J., Korth, H., Slavin, J. A., Purucker, M. E., & Solomon, S. C. (2012). Observations of Mercury's northern cusp region with MESSENGER's magnetometer. *Geophysical Research Letters*, *39*(8), L08112. https://doi.org/10.1029/2012gl051472

Xu, Y., Arridge, C. S., Yao, Z. H., Zhang, B., Ray, L. C., Badman, S. V., et al. (2024). In situ evidence of the magnetospheric cusp of Jupiter from Juno spacecraft measurements. *Nature Communications*, *15*(1), 6062. https://doi.org/10.1038/s41467-024-50449-z

Zhao, J.-T., Zong, Q.-G., Yue, C., Sun, W.-J., Zhang, H., Zhou, X.-Z., et al. (2022). Observational evidence of ring current in the magnetosphere of Mercury. *Nature Communications*, *13*(1), 924. https://doi.org/10.1038/s41467-022-28521-3

Zhong, J. (2024). Key issues on magnetic reconnection at Mercury. *Earth and Planetary Physics*, *8*(5), 673–685. https://doi.org/10.26464/epp2024065

Zhong, J., Lee, L.-C., Slavin, J. A., Zhang, H., & Wei, Y. (2023). MESSENGER observations of reconnection in Mercury's magnetotail under strong IMF forcing. *Journal of Geophysical Research: Space Physics*, *128*(2), e2022JA031134. https://doi.org/10.1029/2022JA031134

Zhong, J., Lee, L. C., Wang, X. G., Pu, Z. Y., He, J. S., Wei, Y., & Wan, W. X. (2020). Multiple X-line reconnection observed in Mercury's magnetotail driven by an interplanetary coronal mass ejection. *The Astrophysical Journal*, *893*(1), L11. https://doi.org/10.3847/2041-8213/ab8380

Zhong, J., Wan, W. X., Slavin, J. A., Wei, Y., Lin, R. L., Chai, L. H., et al. (2015). Mercury's three-dimensional asymmetric magnetopause. *Journal of Geophysical Research: Space Physics*, *120*(9), 7658–7671. https://doi.org/10.1002/2015ja021425

Zhong, J., Xie, L., Lee, L.-C., Slavin, J. A., Raines, J. M., Dewey, R. M., et al. (2024). North–south plasma asymmetry across Mercury's near-tail current sheet. *Geophysical Research Letters*, *51*(1), e2023GL106266. https://doi.org/10.1029/2023gl106266

Zomerdijk-Russell, S., Masters, A., Sun, W. J., Fear, R. C., & Slavin, J. A. (2023). Does reconnection only occur at points of maximum shear on Mercury's dayside magnetopause? *Journal of Geophysical Research: Space Physics*, *128*(11), e2023JA031810. https://doi.org/10.1029/2023ja031810

Zurbuchen, T. H., Raines, J. M., Slavin, J. A., Gershman, D. J., Gilbert, J. A., Gloeckler, G., et al. (2011). MESSENGER observations of the spatial distribution of planetary ions near Mercury. *Science (New York, N.Y.)*, *333*(6051), 1862–1865. https://doi.org/10.1126/science.1211302